

# A Robust Prototype-Based Network with Interpretable RBF Classifier Foundations

Sascha Saralajew,<sup>1</sup> Ashish Rana,<sup>1</sup> Thomas Villmann,<sup>2</sup> and Ammar Shaker<sup>1</sup>

<sup>1</sup>NEC Laboratories Europe, Germany

<sup>2</sup>University of Applied Sciences Mittweida, Germany

{sascha.saralajew, ashish.rana, ammar.shaker}@neclab.eu, villmann@hs-mittweida.de

## Abstract

Prototype-based classification learning methods are known to be inherently interpretable. However, this paradigm suffers from major limitations compared to deep models, such as lower performance. This led to the development of the so-called deep Prototype-Based Networks (PBNs), also known as prototypical parts models. In this work, we analyze these models with respect to different properties, including interpretability. In particular, we focus on the Classification-by-Components (CBC) approach, which uses a probabilistic model to ensure interpretability and can be used as a shallow or deep architecture. We show that this model has several shortcomings, like creating contradicting explanations. Based on these findings, we propose an extension of CBC that solves these issues. Moreover, we prove that this extension has robustness guarantees and derive a loss that optimizes robustness. Additionally, our analysis shows that most (deep) PBNs are related to (deep) RBF classifiers, which implies that our robustness guarantees generalize to shallow RBF classifiers. The empirical evaluation demonstrates that our deep PBN yields state-of-the-art classification accuracy on different benchmarks while resolving the interpretability shortcomings of other approaches. Further, our shallow PBN variant outperforms other shallow PBNs while being inherently interpretable and exhibiting provable robustness guarantees.

## 1 Motivation and Context

Two principal streams exist in the field of explainable machine learning: (1) post-processing methods (post-hoc approaches) that try to explain the prediction process of an existing model, such as LIME and SHAP (see Marcinkevičs and Vogt 2023, for an overview), and (2) the design of machine learning methods with inherently interpretable prediction processes (Rudin 2019). While the former could create non-faithful explanations due to only approximating the output distribution of a black box model without explaining its internal logic, it is claimed that inherently interpretable methods always generate faithful explanations (Rudin 2019). According to Molnar (2022), a model is called *interpretable* if its behavior and predictions are understandable to humans. Moreover, when the provided explanations lead to a correct interpretation of the model, this interpretation enriches the user (or developer) with an understanding of how the model works, how it can be fixed or improved, and whether it can be trusted (Ribeiro, Singh, and Guestrin 2016).

A well-known category of interpretable models for classification tasks is (shallow) Prototype-Based Networks (PBN) such as LVQ (e. g., Biehl, Hammer, and Villmann 2016). These models are interpretable because (1) the learned class-specific prototypes<sup>1</sup> are either from the input space or can be easily mapped to it; belonging to the input space helps summarize the differentiating factors of the input data and provides trusted exemplars for each class, (2) the dissimilarity computations are given by human comprehensible equations such that differences between inputs and learned prototypes can be understood, (3) the classification rule based on the dissimilarities is intelligible (e. g., winner-takes-all principle); see Bancos et al. (2020) for an interpretability application. Despite being interpretable, these models also face limitations: (1) The number of parameters becomes large on complex data since the prototypes are class-specific and are defined in the input space.<sup>2</sup> (2) The classification performance is behind that of deep neural architectures as the dissimilarity functions and the classification rules are straightforward to ensure interpretability (Villmann, Bohnsack, and Kaden 2017).

To fix these limitations, researchers investigated the integration of prototype-based classification heads with deep neural feature extractors to build deep interpretable PBNs and designed numerous architectures such as ProtoPNet (Chen et al. 2019), ProtoPool (Rymarczyk et al. 2022), CBC (Classification-By-Components; Saralajew et al. 2019), and PIPNet (Nauta et al. 2023). The generated results of these models are impressive as they achieve state-of-the-art classification accuracy on fine-grained image classification, and some show a good performance in rejecting Out-Of-Distribution (OOD) examples (e. g., PIPNet). The high-level structure of these models follows the same principles (see Fig. 1): (1) embedding of the input data in a latent space by a Neural Network (NN), denoted as feature extractor backbone; (2) measuring the dissimilarity (or similarity) between the embedding and the latent prototypes; (3) prediction computation after aggregating the dissimilarities by a shallow model (realizes the classification rule), denoted as classification head. In this paradigm, the differences between the

<sup>1</sup>Usually, prototypes are class-specific, and components, centers, or centroids are class-unspecific.

<sup>2</sup>A ResNet50 on ImageNet has 26 M parameters, whereas an LVQ model with one prototype per class has 150 M.

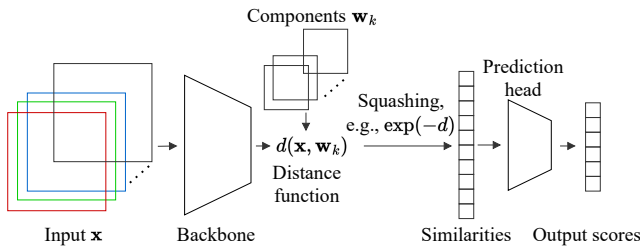


Figure 1: General architecture of deep PBNs.

proposed architectures are often subtle, such as imposing sparsity, the usage of negative reasoning, and whether they can be used as a shallow model. Moreover, all architectures are supposed to generate interpretable models. But is this genuinely accurate?

In this paper, we investigate PBNs and make the following contributions:

1. We show that deep PBNs are related to deep RBF classifiers. Building on this finding, we explain why these models are effective for OOD detection.
2. We discuss why current *deep* PBNs are not interpretable and demonstrate how the interpretability level of the models varies between the different architectures.
3. Building on CBCs and their relation to RBF networks, we design a prototype-based classification head that can use negative reasoning in a sound probabilistic way and fixes the interpretability issue of other heads.
4. We derive robustness bounds for our classification head (shallow PBN), including a loss that provably optimizes robustness. Further, the relation shown gives the first loss that optimizes the robustness of RBF classifiers.

The paper’s outline is as follows: In Sec. 2, we review deep PBNs and discuss their relation to RBF networks (Broomhead and Lowe 1988) and several properties. Based on the identified shortcomings, in Sec. 3, we propose an extension of CBC so that the interpretability is sound and negative reasoning is used. Additionally, we show that the shallow version of this architecture has provable robustness guarantees. Sec. 4 presents the experimental evaluation of our claims. Finally, a discussion and conclusion are presented.

## 2 Review of Deep Prototype-based Networks

In the following section, we review the differences between deep PBNs and show their relation to RBF networks. Thereafter, we discuss the interpretability of these methods using the established relation. Later, we explain why PBNs are suitable for OOD detection and analyze the role of negative reasoning.

**Differences between the architectures and their relation to RBF networks.** Fig. 1 shows the general architecture of most deep PBNs. We use the shown building blocks to characterize existing approaches in Tab. 1 along the following dimensions:

- **Backbone:** Single, multiple, or Siamese feature extractor, and whether the method has been tested without a feature extractor (shallow model).
- **Latent prototypes:** Whether the prototypes are defined in the input or the latent space and if they are back-projected to training samples (Chen et al. 2019). This dimension also indicates if prototypes are class-specific.
- **Similarity:** The used similarity function. RBF refers to the standard squared exponential kernel. If a different non-linear function is used to construct the RBF, it is specified in parenthesis. Note that all RBFs use the Euclidean norm.
- **Linear layer constraints:** The constraints on the final linear prediction layer or the stated approach to compute the output if no linear output layer is used. The  $l_1$  regularization is only applied to connections that connect similarity scores (slots, etc.) with incorrect classes.
- **Single loss term:** Whether multiple loss terms are used.
- **Main contribution:** The primary contribution of the proposed architecture compared to previous work.

We identified the following architectures by reviewing top-tier venue papers: LeNet5 (LeCun et al. 1998), ProtoPNet, CBC, Hierarchical ProtoPNet (Hase et al. 2019), ProtoAttend (Arik and Pfister 2020), ProtoTree (Nauta, van Bree, and Seifert 2021), ProtoPShare (Rymarczyk et al. 2022), TesNet (Wang et al. 2021), Deformable ProtoPNet (Donnelly, Barnett, and Chen 2022), ProtoPool, and PIPNet. Moreover, we added LucidPPN (Pach et al. 2024) and ProtoViT (Ma et al. 2024) as it is the most recent publication in the field.

Considering Fig. 1, we realize that the head of a deep PBN is an RBF network if a linear layer is used for prediction. Combined with a feature extractor, we obtain *deep RBF networks* (e. g., Asadi et al. 2021). Notably, the first deep PBN is LeNet5, where RBF heads are used to measure the similarity between inputs and the so-called “model” (prototype) of the class. Starting with ProtoPNet, the existing architectures (see Tab. 1) build on each other (except for CBC and ProtoAttend), and almost all use an RBF network with some constraints or regularizers as classification heads. Consequently, changes between the architectures are incremental, and concepts persist for some time once introduced. Recently, researchers abandoned the idea of back-projecting prototypes and started using dot products instead of RBF functions, which implicitly defines prototypes as convolutional filter kernels (PIPNet, LucidPPN).

**On the interpretability of deep PBNs.** Using the definition of interpretability in Sec. 1 and the relation to RBF networks, we discuss the interpretability of deep PBNs. First, it should be noted that RBF networks and shallow PBNs learn representations in the input space (centroids and prototypes, respectively), and both use these representations to measure the (dis-)similarity to given samples. At the same time, these two paradigms differ in two aspects: (1) RBFs’ usage of non-class specific centroids and (2) PBNs’ usage of the human-comprehensible winner-takes-all rule instead of a linear predictor over the prototypes.

The first aspect overcomes the Limitation (1) mentioned in Sec. 1 without harming the interpretability. The second

	Backbone	Latent Proto.	Similarity	Linear Layer Constraints	Single Loss	Main Contribution
<b>LeNet5</b>	single	yes	RBF	none	no	CNN with RBF head
<b>ProtoPNet*</b>	single	yes*	RBF (log)	$l_1$ reg.	no	(deep) NN with prototype classification head
<b>CBC*</b>	Siamese*	no	RBF or ReLU-cosine	probabilistic	yes	negative/positive/indefinite reasoning
<b>Hier. ProtoPNet</b>	single	yes*	RBF (log)	$l_1$ reg.	no	hierarchical classification
<b>ProtoAttend*</b>	Siamese	no	relational attention	none	no	attention for prototype selection
<b>ProtoTree</b>	single	yes*	RBF	(soft) tree*	yes	tree upon similarities
<b>ProtoPShare</b>	single	yes*	RBF (log)	$l_1$ reg.	no	prototype sharing between classes
<b>TesNet</b>	single	yes*	dot-product	$l_1$ reg.	no	orthogonal prototypes
<b>Def. ProtoPNet</b>	single	yes*	RBF (cosine)	$l_1$ reg.	no	deformable prototypes (shift correction)
<b>ProtoPool</b>	single	yes*	RBF (focal similarity)	$l_1$ reg.	no	differentiable prototype selection
<b>PIPNet</b>	single	yes	softmax dot product	non-negative	no	self-supervised pre-training
<b>LucidPPN</b>	multiple	yes	sigmoid dot product	average*	no	color and shape backbone
<b>ProtoViT</b>	single	yes*	scaled sum of cosine	$l_1$ reg.	no	deformable prototypes through vision transformer
<b>Ours</b>	single*	yes	RBF or softmax dot product	probabilistic	yes	trainable priors and provable robustness

Table 1: Characterization of existing architectures along the specified dimensions. Note that the order is chronological. Methods that are not directly based on the previously published methods are marked with an asterisk. The asterisk in the remaining columns stands for the ability to omit the feature extractor in Backbone, the usage of back-projection of latent prototypes in Latent Prototype, and an alternative approach for the output computation in Linear Layer Constraints (i. e., no application of a linear layer with a regularization or constraint). The italic typeface in Latent Prototype states that the prototypes are class-specific.

aspect poses a problem for interpretation, which explains the lack of studies applying RBF networks for interpretable machine learning. The problem starts with the unconstrained weights in the linear layer, which lead to unbounded and incomparable scores (e. g., it is unclear how to interpret a high score or weight). Further, this could result in situations where the closest (most similar) centroids do not contribute the most to the classification score compared to less similar centroids that are overemphasized by large weights. Hence, this breaks the paradigm that the most similar centroids (or prototypes) define the class label.

What does this imply for deep PBNs? First, the interpretation of the classification head suffers from the same difficulties as an RBF network if no appropriate constraints are applied (e. g., the average computation of LucidPPN). Therefore, the most similar prototypes for an input do not necessarily define the class label. For example, PIPNet trained on CUB (Wah et al. 2011) uses average weights of 14.1 for class blue jay and 8.7 for green jay. This indicates that PIPNet overemphasizes small similarity values so that the interpretation of the influential prototypes could be incorrect; further results in Sec. 4. Second, since the similarity is computed in a latent space defined by a deep NN, it is unclear why two samples are close or distant due to the black-box nature of deep NNs. Thus, it is *misleading* to denote a deep PBN as interpretable. In the best case, it can be denoted as *partially*

*interpretable* as it gives insights into the final classification step, assuming that the classification head is well-designed. Note that the interpretability of these methods is also questioned by others (e. g., Hoffmann et al. 2021; Pazzani et al. 2022; Sacha et al. 2024; Wolf et al. 2024).

**On the OOD detection properties.** In CBC (rejection of predictions), Hierarchical ProtoPNet (novel class detection), ProtoAttend (OOD detection), and PIPNet (OOD detection), it was shown that deep PBNs are suitable for identifying OOD samples. This ability can be attributed to the RBF architecture if the model is clearly related to RBF models. Hein, Andriushchenko, and Bitterwolf (2019) proved that RBF networks produce low-confidence predictions when *a given sample is far away from all centroids (prototypes)* because the applied softmax squashing enforces the predictions of all classes to be uniform. Van Amersfoort et al. (2020) built on this idea and empirically showed that deep feature extractors with an RBF head and a winner-takes-all rule (so a deep PBN) can be used for uncertainty estimation and, thus, OOD detection. The published results for deep PBNs also confirm this property van Amersfoort et al. (2020) observed. Empirically, this property transfers beyond RBF-related architectures, as architectures like PIPNet show a remarkable OOD performance using a non-RBF similarity.

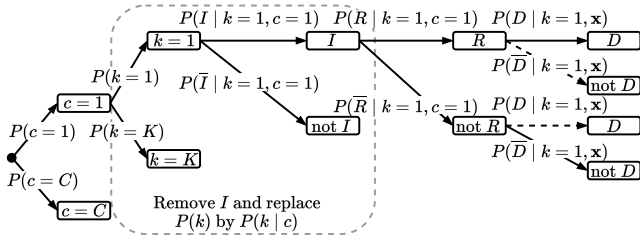


Figure 2: Probability tree diagram of the original CBC with the changes we propose for our extension in the gray box.

**The role of negative reasoning.** Positive reasoning is well-defined as retrieving evidence of a given class from present features, but the literature does not reach a consensus about negative reasoning. In CBC, it means the retrieval of evidence from absent features. In contrast, in ProtoPNet, this refers to the reduction of the final score due to a negative weight associated with an active prototype. Other methods in the literature either penalize negative reasoning (e. g., ProtoPNet) by a regularization term or avoid it by a constraint (e. g., PIPNet); see the Constraints column in Tab. 1. The challenge posed by negative reasoning in these architectures is mainly about interpretation, as it is not an intuitive reasoning principle of humans (according to Chen et al. 2019) and complicates the explanation strategies. In a notable contrast, in CBC, inspired by cognitive science results (e. g., Hsu et al. 2017), the authors modeled negative reasoning from a probabilistic perspective, making its interpretation mathematically sound. For the remainder of the paper, we refer by negative reasoning to the retrieval of evidence from features that have to be absent.

### 3 Classification-by-Components Networks

We now review the original CBC architecture and show its limitations. Based on that, we propose our CBC—simply denoted as CBC and the old version is denoted as *original CBC*—that overcomes these limitations and realizes a strong link to RBF networks. Then, we show how a CBC can be learned efficiently and derive robustness lower bounds.

**Review of the original CBC method.** Components are the core concept of the original CBC, where a component is a pattern that contributes to the classification process by its presence (positive reasoning; the component must be close) or absence (negative reasoning; the component must be far) without being tied to a specific class label. A component can also abstain from the classification process, which is called indefinite reasoning (modeled via importance). The original CBC is based on a probability tree diagram to model the interaction between the detection of components in input samples and the usage of detection responses to model the output probability (called reasoning). The probability tree, Fig. 2, employs five random variables:  $c$ , the class label;  $k$ , the component;  $I$ , the importance of a component (binary);  $R$ , the requiredness for reasoning (binary);  $D$ , the detection of a component (binary). The probability tree constructs the following:  $P(k)$ , the prior of the  $k$ -th component to appear;  $P(I|k, c)$  and

$P(R|k, c)$  are the importance and the requiredness probabilities of the  $k$ -th component for the class  $c$ ;  $P(D|k, \mathbf{x})$ , the detection probability of the  $k$ -th component in the input  $\mathbf{x}$ .  $P(\bar{D}|k, \mathbf{x})$  is the complementary probability, that is, *not* detecting the  $k$ -th component in  $\mathbf{x}$ . An agreement  $A$  is a path in the tree (see solid lines in Fig. 2) that depicts the positive influence of the  $k$ -th component on class  $c$  by either being detected ( $D$ ) and required ( $R$ ) or not detected ( $\bar{D}$ ) and not required ( $\bar{R}$ ). The output probability  $p_c(\mathbf{x}) = P(A|I, \mathbf{x}, c)$  for class  $c$  is derived from the agreement  $A$  using the following expression:

$$\frac{\sum_k (P(R, I|k, c) P(D|k, \mathbf{x}) + P(\bar{R}, I|k, c) P(\bar{D}|k, \mathbf{x})) P(k)}{\sum_k (P(R, I|k, c) + P(\bar{R}, I|k, c)) P(k)}. \quad (1)$$

The defined probabilities and components are learned by minimizing the margin loss (maximizing the probability gap)

$$\min \left\{ \max_{c' \neq y} p_{c'}(\mathbf{x}) - p_y(\mathbf{x}) + \gamma, 0 \right\}, \quad (2)$$

with  $\gamma \in [0, 1]$  being the margin value,  $y$  being the correct class label of  $\mathbf{x}$ , and  $c'$  being any class label other than  $y$ . The model can be used without or with a feature extractor (see Fig. 1); that is, the distance computation occurs in the learned latent space. An original CBC without a feature extractor realizes an extension of traditional PBNs, overcoming Limitation (1) while posing new difficulties.

The architecture is difficult to train as it often converges to a bad local minimum (see Sec. 4), and the explanations can be counterintuitive. To see this, note that  $P(R, I|k, c) + P(\bar{R}, I|k, c) + P(\bar{I}|k, c) = 1$  for each  $k$ . Thus, one can scale the reasoning probabilities  $P(R, I|k, c)$  and  $P(\bar{R}, I|k, c)$  in Eq. (1) by any factor  $\alpha > 0$  as long as  $P(R, I|k, c), P(\bar{R}, I|k, c) \in [0, 1]$  remains valid without changing the output probability  $p_c(\mathbf{x})$ . Assuming that  $p_c(\mathbf{x}) = 1$ , this result can be obtained from nearly zero reasoning probabilities, giving confident predictions from infinitesimal reasoning evidence. This contradicts the design principle of the original CBC approach, as  $p_c(\mathbf{x}) = 1$  should only be generated if the model is certain in its reasoning. At the same time, this result implies that the optimal output ( $p_c(\mathbf{x}) = 1$ ) is not unique with a wide range of flawed feasible solutions, thus causing the model to converge to bad local minima.

**Our extension of the original CBC method.** In CBC, both problems mentioned above are caused by the indefinite reasoning probability  $P(\bar{I}|k, c)$  together with the component prior  $P(k)$ . These probabilities model the extent to which a component is used in the classification process; hence, they both serve the same purpose, as confirmed by fixing  $P(k)$  to be uniform in the original CBC. Removing  $P(\bar{I}|k, c)$  from the model eliminates the problematic model’s tolerance towards scaling by a factor  $\alpha$ . Still, it causes missing support for allowing components to remain irrelevant (to abstain), as explained by Saralajew et al. (2019) in Figure 1. Similarly, allowing the prior  $P(k)$  to be trainable does not generalize to cover the property of class-specific component priors.

We now present our modification to the original CBC to overcome the difficulties. We propose to remove the impor-

tance variable  $I$  and substitute it with the *trainable class-wise component* prior  $P(k | c)$ , see Fig. 2. The output probability  $p_c(\mathbf{x}) = P(A | \mathbf{x}, c)$ , using the agreement, becomes

$$P(A | \mathbf{x}, c) = \sum_k (P(R, D | \mathbf{x}, c, k) + P(\bar{R}, \bar{D} | \mathbf{x}, c, k)) P(k | c) = \sum_k (P(R | c, k) P(D | \mathbf{x}, k) + P(\bar{R} | c, k) P(\bar{D} | \mathbf{x}, k)) P(k | c) \quad (3)$$

We introduce the following notations:

- The requiredness possibility vector  $\mathbf{r}_c \in [0, 1]^K$  contains the probabilities  $P(R | c, k)$  for all  $k$ .
- The detection possibility vector  $\mathbf{d}(\mathbf{x}) \in [0, 1]^K$  contains the probabilities  $P(D | \mathbf{x}, k)$  for all  $k$ .
- The component prior probability vector  $\mathbf{b}_c \in [0, 1]^K$  contains the probabilities  $P(k | c)$  for all  $k$ .

Note that  $\sum_k b_{c,k} = \sum_k P(k | c) = 1$ , which is not necessarily true for  $\mathbf{d}$  and  $\mathbf{r}_c$ . Now, Eq. (3) can be written as

$$p_c(\mathbf{x}) = (\mathbf{r}_c \circ \mathbf{d}(\mathbf{x}) + (\mathbf{1} - \mathbf{r}_c) \circ (\mathbf{1} - \mathbf{d}(\mathbf{x})))^T \mathbf{b}_c, \quad (4)$$

where  $\circ$  is the Hadamard product. The detection probability can be any suitable function, like the following RBF:<sup>3</sup>

$$P(D | \mathbf{x}, k) = \exp\left(-\frac{d_E(\mathbf{x}, \mathbf{w}_k)}{\sigma_k}\right), \quad (5)$$

where  $d_E$  is the Euclidean distance,  $\sigma_k$  is the (trainable) component-dependent temperature, and  $\mathbf{w}_k$  is the vector representation of component  $k$ . Using Eq. (4), similarly to other deep PBNs, the architecture is trained by optimizing the parameters of the components  $\mathbf{w}_k$ , the prior probabilities  $\mathbf{b}_c$ , and the reasoning possibility vector  $\mathbf{r}_c$ . For the optimization, the margin loss Eq. (2) can be used.

**Learning the parameters in CBC models.** When adopted without a feature extractor, learning a CBC model realizes an extension of shallow PBNs using components instead of prototypes (Limitation (1) in Sec. 1) and constitutes an interpretable RBF network (fixes the interpretability issues mentioned in Sec. 2). Note that in the computation of Eq. (3), the requiredness probabilities  $P(R | c, k)$  and the component prior probabilities  $P(k | c)$  occur jointly and provide the *reasoning probabilities*  $P(R, k | c) = P(R | c, k) P(k | c)$ . This simplification makes the association to RBF networks more explicit by rewriting Eq. (3) as  $p_c(\mathbf{x}) = \sum_k \alpha_k P(D | \mathbf{x}, k) + \beta$ , where  $\alpha_k = P(R, k | c) - P(\bar{R}, k | c)$  is the weight and  $\beta = \sum_k P(\bar{R}, k | c)$  is the bias.

Moreover, the network is simplified during training, and only the reasoning probabilities  $P(R, k | c)$  are learned, leading to fewer multiplications of trainable parameters (simpler gradient computation graph). In practice, the trainable parameters  $P(R, k | c)$  and  $P(\bar{R}, k | c)$  take the form of the vector

<sup>3</sup>The detection probability must be a similarity measure  $\mathbb{R}^n \times \mathbb{R}^n \rightarrow [0, 1]$  such that  $\mathbf{x} = \mathbf{w}_k$  implies a similarity of 1.0.

$\mathbf{v}_c \in \mathbb{R}^{2K}$  for each class, which is normalized to achieve  $\sum_i \text{softmax}(\mathbf{v}_c)_i = 1$ . Within  $\mathbf{v}_c$ , the first half of the parameters represent the positive and the second half the negative reasoning probabilities. The computation of  $p_c(\mathbf{x})$  becomes  $\mathbf{v}_c^T [\mathbf{d}(\mathbf{x}), (\mathbf{1} - \mathbf{d}(\mathbf{x}))]$ , where the detection and no detection vectors are concatenated into one vector. Consequently, and again, the model realizes an RBF network that uses negative reasoning. If we block negative reasoning by setting the respective probabilities to zero, we obtain an RBF network with class-wise weights constrained while solving the interpretability issues from Sec. 2.

**The proven robustness of the CBC architecture.** In this section, we derive the robustness lower bound. We analyze the stability of the classification decision when *no* feature extractor is applied; with a feature extractor, the same stability analysis applies in the latent space. Given a data point  $\mathbf{x} \in \mathbb{R}^n$  with the target label  $y$ , the input is correctly classified if the probability gap is positive:

$$p_y(\mathbf{x}) - \max_{c' \neq y} p_{c'}(\mathbf{x}) > 0. \quad (6)$$

Robustness comes from deriving a non-trivial lower bound for the maximum applicable perturbation  $\boldsymbol{\varepsilon}^* \in \mathbb{R}^n$  without having the predicted class label of  $\mathbf{x}$  changed, that is,

$$p_y(\mathbf{x} + \boldsymbol{\varepsilon}^*) - \max_{c' \neq y} p_{c'}(\mathbf{x} + \boldsymbol{\varepsilon}^*) > 0; \quad (7)$$

the strength of the perturbation is given by  $\|\boldsymbol{\varepsilon}^*\|$ . Thm. 1 derives a lower bound of  $\|\boldsymbol{\varepsilon}^*\|$  for detection probability functions of the form Eq. (5) where  $d_E$  is any distance function induced by the selected norm  $\|\cdot\|$ . Thm. 2 extends this derivation to squared norms (e. g., Gaussian kernel) so that the result can be applied to standard Gaussian RBF networks using the established relation.

**Theorem 1.** *The robustness of a correctly classified sample  $\mathbf{x}$  with class label  $y$  is lower bounded by*

$$\|\boldsymbol{\varepsilon}^*\| \geq \underbrace{\kappa \min_{c' \neq y} \left( \ln \left( \frac{B_{c'} + \sqrt{B_{c'}^2 - 4A_{c'}C_{c'}}}{2A_{c'}} \right) \right)}_{=: \delta} > 0, \quad (8)$$

when  $A_{c'} \neq 0$ , where

$$A_{c'} = ((\mathbf{r}_y - \mathbf{1}) \circ \mathbf{b}_y - \mathbf{r}_{c'} \circ \mathbf{b}_{c'})^T \mathbf{d}(\mathbf{x}),$$

$$B_{c'} = (\mathbf{1} - \mathbf{r}_y)^T \mathbf{b}_y - (\mathbf{1} - \mathbf{r}_{c'})^T \mathbf{b}_{c'},$$

$$C_{c'} = (\mathbf{r}_y \circ \mathbf{b}_y - (\mathbf{r}_{c'} - \mathbf{1}) \circ \mathbf{b}_{c'})^T \mathbf{d}(\mathbf{x}),$$

and  $\kappa = \sigma_{\min} = \min_k \sigma_k$ .

All proofs can be found in Appx. B. Additionally, it can be shown that  $\delta$  in Eq. (8) is negative if the sample is incorrectly classified. Therefore,  $\delta$  in Eq. (8) can be used as a loss function to optimize the model for stability. Of course, this loss can be clipped at a threshold  $\gamma > 0$  so that the network optimizes for robustness of at most  $\gamma$ .

**Theorem 2.** *If we use the standard RBF kernel (squared norm), then Eq. (8) becomes  $\|\boldsymbol{\varepsilon}^*\| \geq -\frac{\beta}{3} + \sqrt{\frac{\beta^2}{9} + \delta} > 0$  with  $\kappa = \frac{\sigma_{\min}}{3}$  and  $\beta = \max_k d(\mathbf{x}, \mathbf{w}_k)$ .*

Again, this result helps to construct a loss function that maximizes robustness. For standard Gaussian kernel RBF networks with class-wise weights  $\mathbf{v}_c$  constrained to probability vectors, the main part  $\delta$  of the function is simplified to

$$\frac{\sigma_{\min}}{6} \min_{c' \neq y} \ln \left( \frac{\mathbf{v}_{y'}^T \mathbf{d}(\mathbf{x})}{\mathbf{v}_c^T \mathbf{d}(\mathbf{x})} \right), \quad (9)$$

a log-likelihood ratio loss (e. g., Seo and Obermayer 2003).

**The robustness with alternative distance functions.** Similar to other shallow PBNs, CBCs can use alternative distance functions such as the Mahalanobis distance or the tangent distance (e. g., Haasdonk and Keysers 2002)

$$d_T(\mathbf{x}, S) = \min_{\theta \in \mathbb{R}^r} d_E(\mathbf{x}, \mathbf{w} + \mathbf{W}\theta), \quad (10)$$

where  $S = \{\mathbf{w} + \mathbf{W}\theta \mid \theta \in \mathbb{R}^r\}$  is a trainable  $r$ -dimensional affine subspace with  $\mathbf{W}$  being a basis. By learning affine subspaces instead of points for the components, the discriminative power of the architecture is significantly improved (Saralajew, Holdijk, and Villmann 2020). Moreover, if this distance is used in a deep PBN, it realizes an extension of TesNet by learning disentangled concepts (each basis vector in  $\mathbf{W}$  is a basis concept) but measures the distance with respect to  $d_T$ . See Appx. A for further details about this distance. Next, Thm. 3 extends the lower bound derived in Thm. 1 for the tangent distance.

**Theorem 3.** *If we use the tangent distance in Eq. (5), Eq. (8) holds with  $\kappa = \frac{1}{2}\sigma_{\min}$  and  $\|\cdot\|$  being the Euclidean norm.*

A similar result was proven for LVQ with the tangent distance (Saralajew, Holdijk, and Villmann 2020).

**Final remarks.** Our proposed CBC resolves the original approach’s drawbacks. Further, the architecture can be derived from RBF networks by introducing interpretability constraints and negative reasoning. The method can be used as a head for deep PBNs or as a standalone for prototype-based classification learning. In all cases, the interpretability of the learned weights is guaranteed by the relation to the probability events. Appx. C presents further theoretical results.

## 4 Experiments

In this section, we test our CBC and the presented theories: (1) We analyze the accuracy and interpretability of our CBC and compare it to PIPNet. (2) We compare shallow CBCs with other shallow models, such as the original CBC. (3) To demonstrate our theorems, we analyze the adversarial robustness of shallow PBNs. Note that all accuracy results are reported in percentage; we train each model five times, and report the mean and standard deviation.<sup>4</sup>

**Interpretability and performance assessment: Comparison with PIPNet.** We evaluate the performance of CBC in comparison with PIPNet and the state-of-the-art deep PBN ProtoPool and ProtoViT<sup>5</sup> (CaiT-XXS 24; best-performing

<sup>4</sup>The source code is available at <https://github.com/si-cim/cbc-aaai-2025>.

<sup>5</sup>It was not published when the submission draft for AAAI was written.

	CUB	CARS	PETS
PIPNet	84.3 ± 0.2	88.2 ± 0.5	92.0 ± 0.3
ProtoPool	85.5 ± 0.1	88.9 ± 0.1	87.2* ± 0.1
ProtoViT	85.8 ± 0.2	92.4 ± 0.1	93.3* ± 0.2
CBC	<b>87.8 ± 0.1</b>	<b>93.0 ± 0.0</b>	<b>93.9 ± 0.1</b>
CBC pos. reas.	28.6 ± 0.8	25.3 ± 2.3	69.5 ± 5.1

Table 2: Test accuracy on different benchmark datasets. If available, we copied the accuracy values from the respective papers. Otherwise, we computed them (marked by an asterisk).

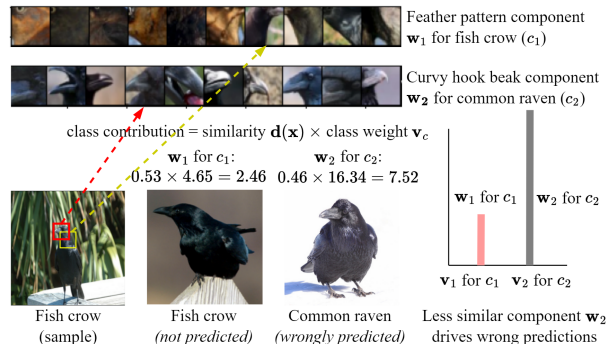


Figure 3: Fish crow gets incorrectly classified as common raven by PIPNet because of the overemphasis of weights.

backbone). Since CBC can work with any backbone, we use PIPNet’s ConvNeXt-tiny (Liu et al. 2022) architecture, the best-performing one from PIPNet. We extend PIPNet by only replacing the final classification layer with a CBC head. This way, the components become implicitly defined by the weights of the last convolutional layer with softmax-normalized dot product as a similarity. For training, we follow the pre-training protocol from PIPNet and extend the classification step using our proposed margin loss Eq. (2) with  $\gamma = 0.025$ . We benchmark the methods using CUB, CARS (Krause et al. 2013), and PETS (Parkhi et al. 2012) datasets.

The test accuracy results of our model sets new benchmarks as shown in Tab. 2. To analyze the reason for this accuracy gain, we trained another PIPNet, replacing the ReLU constraint on the classification weights with a softmax. By this, we avoid the mentioned interpretability issues and obtain a CBC restricted to positive reasoning only (CBC pos. reas.). This model constantly scores behind CBC with negative reasoning. Hence, the accuracy gain can be attributed to the usefulness of negative reasoning.

To assess the interpretability, we use PIPNet’s approach to determine the top-10 component visualizations from the training dataset. Fig. 3 shows an example that is wrongly classified by PIPNet due to the overemphasis of specific weights. Ravens have curved hook-like beaks and regions of larger feathers, whereas crows have streamlined beaks and small feathers. The crow depicted in this figure is wrongly classified as a raven because the most similar component  $\mathbf{w}_1$  (feather), which correctly indicates that it is a crow, is overshadowed by the less similar component  $\mathbf{w}_2$  (hook-like

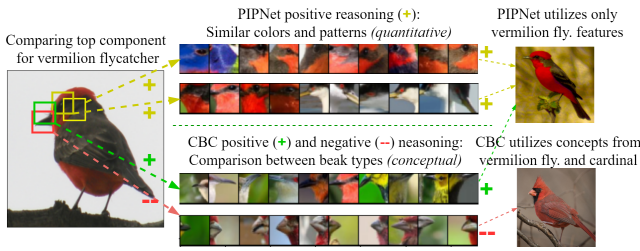


Figure 4: The comparative analysis of PIPNet and CBC for the vermilion flycatcher, where negative reasoning is used.

beak) that has a higher weight. This example confirms our hypothesis from Sec. 2 that non-normalized weights hinder interpretability by preventing the most relevant prototypes from influencing the prediction.

Fig. 4 shows an example of positive and negative reasoning to distinguish between two close bird species. PIPNet uses positive reasoning to match based on regions with similar colors or color contrasts, focusing less on contextual understanding. CBC focuses on learning concepts like the pointed streamlined beak irrespective of the bird species or color pattern patches. As this component is similar to the beak of the depicted bird (vermillion flycatcher), it contributes to the classification as a vermillion flycatcher (positive reasoning). At the same time, CBC distinguishes the vermillion flycatcher from a similar species in appearance, the cardinal, by using negative reasoning with the absence of the cardinal’s broad beak.

To quantitatively assess how different components are used across different classes by learning class-specific component priors, we computed the Jensen–Shannon divergence between the priors of each pair of bird classes. The divergence depicts how the distributions of the components’ priors differ across classes. The following shows this for the Black-footed Albatross compared to three other species: Laysan Albatross 1.1, Crested Auklet 5.1, and Least Auklet 4.4. These results indicate a smaller divergence to the Laysan Albatross, a close relative from the same family, and greater divergences to more distantly related species. This demonstrates that our approach generally shares components across similar classes while using different components for others. Again, this result underlines the importance of learning class-specific component priors. Appx. D.1 presents model training details, ResNet50 results, and more interpretability results.

**Comparison with shallow models.** In this experiment, we compare CBC with its variants and other baseline models. Namely, we compare with GLVQ (Sato and Yamada 1996), RBF networks, and the original CBC. We also implement RBF networks with softmax layer normalization (RBF-norm) and RBF networks with Tangent Distance (RBF-norm TD); see Eq. (10). We evaluate CBC with the Tangent Distance (CBC TD), with the robustness loss optimization (Robust CBC; see Thm. 1), and with both the robustness loss and the Tangent Distance (Robust CBC TD). All models are trained with the Euclidean distance unless the use of the tangent distance is indicated. The RBF models are trained by the

	Accuracy	Emp. Rob.	Cert. Rob.
GLVQ	80.5 ± 0.6	59.6 ± 0.3	<b>32.3 ± 0.3</b>
RBF	<b>92.2 ± 0.1</b>	61.9 ± 0.9	–
original CBC	81.8 ± 2.0	<b>62.0 ± 1.0</b>	–
CBC	87.4 ± 0.3	68.1 ± 0.7	0.2 ± 0.1
RBF-norm	77.3 ± 0.2	57.7 ± 0.2	0.7 ± 0.0
CBC TD	<b>95.9 ± 0.1</b>	<b>84.5 ± 0.2</b>	0.0 ± 0.0
RBF-norm TD	92.1 ± 0.2	77.8 ± 0.4	0.0 ± 0.0
Robust CBC	87.8 ± 0.3	62.8 ± 0.3	<b>15.2 ± 1.7</b>
Robust CBC TD	91.9 ± 0.3	70.8 ± 0.5	1.6 ± 0.2

Table 3: Test, empirical robust, and certified robust accuracy of shallow PBNs. The robust accuracy is computed for  $\|\epsilon^*\| = 1$ . The top shows prior art, and the bottom shows our models. We put the best accuracy for each category in bold.

cross-entropy loss, GLVQ by the GLVQ-loss function, and non-robust CBC models by the margin loss (Eq. (2) with  $\gamma = 0.3$ ). Each model was trained and evaluated on MNIST (LeCun, Cortes, and Burges 1998). Each CBC and RBF can learn 20 components (or centroids) or two prototypes per class (GLVQ). The CBC models are trained with *two* reasoning concepts per class (two vectors  $\mathbf{r}_c$  and  $\mathbf{b}_c$  per class), component-wise temperatures, and squared Euclidean distances. The class output probability is given by the maximum over the class’s two reasoning concepts. By this, we ensure that, similar to GLVQ, the models can learn two concepts (similar to prototypes) per class.

The results presented in Tab. 3 show that CBC outperforms the original CBC in terms of classification accuracy by over 5%. By inspecting the learned components and probabilities, we observe that the original CBC converges to a sub-optimal solution by learning redundant components and not leveraging the advantage of multiple reasoning concepts per class. Our CBC learns less repetitive components and leverages the two reasoning concepts by learning class-specific components for several classes if required. Additionally, the table shows the advantage of using negative reasoning (cf. CBC and RBF-norm). While the class-wise softmax normalization in RBF-norm transforms it to a CBC with positive reasoning only, it remains outperformed by CBC with negative reasoning by 10%. At the same time, both RBF-norm and CBC remain behind the plain RBF approach, showing how the interpretability constraints reduce the generalization. By using more advanced distance measures such as the tangent distance, we observe that the accuracy improves drastically while still being behind the plain models if they use the tangent distance. See Appx. D.2 for the complete set of results, including the comparison with more shallow models, the component visualizations, training with non-squared distances, and a shallow model with patch components, where the learned reasoning distinguishes between writing styles of the numeral seven.

**Robustness evaluation.** We evaluate the adversarial robustness of the already trained models from the shallow PBN experiments using the AutoAttack framework (Croce and Hein 2020) with the recommended setting and maximum pertur-

bation strength 1.0, see Tab. 3. Additionally, using the result from Thm. 2, we compute the certified robustness by counting how many correctly classified samples have a lower bound greater or equal to 1.0. For GLVQ, we compute the certified robustness by the hypothesis margin (Saralajew, Holdijk, and Villmann 2020). Note that the certified robustness cannot be calculated for RBF and original CBC.

The results show that training a CBC with our robustified loss is possible and yields non-trivial certified robustness. For instance, the Robust CBC outperforms GLVQ, which is provably robust as well, in terms of accuracy and empirical robustness. With respect to the certified robustness, it is behind GLVQ, which can be attributed to the repeated application of the triangle inequality in order to derive the bound. Moreover, it should be noted that the certified robustness of Robust CBC TD is significantly lower than that of Robust CBC. This can be again attributed to the derived lower bound for the tangent distance, where the triangle inequality is applied once more. Hence, the stated bound in Thm. 3 is less tight compared to Thm. 1 and Thm. 2. See Appx. D.3 for the full results, including robustness curves and evaluation of robustified RBF networks using Thm. 2.

## 5 Discussion and Limitations

While we refrain from claiming that our deep model is fully interpretable, we believe it offers partial interpretability, providing valuable insights into the classification process, especially in the final layers. In contrast, the shallow version is inherently interpretable.

Compared to other deep PBNs, our model uses only a single loss term and neither forces the components to be close to training samples nor to be apart from each other. This is beneficial as it simplifies the training procedure drastically since no regularization terms have to be tuned. Even if we only use one loss term, our model converges to valuable components. However, interpreting these components is complex and requires expert knowledge. As a result, especially for deep PBNs, the interpretation could be largely shaped by the user’s mental model, highlighting the importance of quantitative interpretation assessment approaches—something that is still lacking in the field. Additionally, by optimizing the single loss term, our model automatically learns sparse component representations without the issue of the learned representation being excessively sparse (see the additional PIPNet experiments in Appx. D.1).

During the deep model training, we observed that the CBC training behavior can be sensitive to pre-training and initializations. Further, training huge shallow models was challenging, especially when optimizing the robust loss: The model did not leverage all components as they often converged to the same point or failed to use all reasoning vectors if multiple reasoning vectors per class were provided. Additionally, training exponential functions (the detection probability) is sensitive to the selection of suitable temperature values. When we kept them trainable and individual per component, sometimes they became so small that the components did not learn anything even if the components had not converged to a suitable position in the data space. The same happened when we tried to apply exponential functions on top of a

deep feature backbone, making it impossible to train such architectures reliably. These insights provide a foundation for refining our approach in future efforts.

## 6 Conclusion and Outlook

In this paper, we harmonize deep PBNs by showing a solid link to RBF networks. We also show how these models are not interpretable and only achieve partial interpretability in the best case. Inspired by these findings, we derive an improved CBC architecture that uses negative reasoning in a probabilistically sound way and ensures partial interpretability. Empirically, we demonstrate that the proposed deep PBN outperforms existing models on established benchmarks. Besides, the shallow version of our CBC is interpretable and provably robust. The shallow CBC is an attractive alternative to established models such as GLVQ as it resolves known limitations like the use of class-specific prototypes.

Open questions still exist and are left for future work: For example, a modification that prevents components from converging to the same point, along with the integration of spatial knowledge (to avoid global max-pooling), could improve deep PBNs, a challenge that the original CBC partially addressed. Moreover, in our evaluation, we focused on the assessment of our approach using image datasets, which is currently the commonly used benchmark domain for PBNs. However, future work should investigate the application of our approach to other domains, such as time series data. Moreover, to stabilize the training of the detection probability, one should explore the strategies proposed by Ghiasi-Shirazi (2019) or analyze the application of other detection probability functions (note that our theoretical results generalize to exponential functions with an arbitrary base). Finally, it is unclear why all shallow models, including non-robustified ones, exhibit good empirical robustness.

## References

- Arik, S. O.; and Pfister, T. 2020. ProtoAttend: Attention-Based Prototypical Learning. *Journal of Machine Learning Research*, 21(210): 1–35.
- Asadi, K.; Parikh, N.; Parr, R. E.; Konidaris, G. D.; and Littman, M. L. 2021. Deep Radial-Basis Value Functions for Continuous Control. In *Proceedings of the Thirty-Fifth AAAI Conference on Artificial Intelligence – AAAI 2021*, 6696–6704. AAAI Press.
- Bancos, I.; Taylor, A. E.; Chortis, V.; Sitch, A. J.; Jenkinson, C.; Davidge-Pitts, C. J.; Lang, K.; Tsagarakis, S.; Macech, M.; Riester, A.; et al. 2020. Urine steroid metabolomics for the differential diagnosis of adrenal incidentalomas in the EURINE-ACT study: A prospective test validation study. *The Lancet Diabetes & Endocrinology*, 8(9): 773–781.
- Biehl, M.; Hammer, B.; and Villmann, T. 2016. Prototype-based models in machine learning. *Wiley Interdisciplinary Reviews Cognitive Science*, 7(2): 92–111.
- Broomhead, D. S.; and Lowe, D. 1988. Multivariable Functional Interpolation and Adaptive Networks. *Complex Systems*, 2(3).



- Chen, C.; Li, O.; Tao, D.; Barnett, A.; Su, J.; and Rudin, C. 2019. This Looks Like That: Deep Learning for Interpretable Image Recognition. In Wallach, H.; Larochelle, H.; Beygelzimer, A.; d'Alché-Buc, F.; Fox, E.; and Garnett, R., eds., *Advances in Neural Information Processing Systems 32: Proceedings of the Neural Information Processing Systems Conference – NeurIPS 2019*, 8928–8939. Vancouver, BC, Canada: Curran Associates, Inc.
- Croce, F.; and Hein, M. 2020. Reliable evaluation of adversarial robustness with an ensemble of diverse parameter-free attacks. In *Proceedings of the 37th International Conference on Machine Learning – ICML 2020*, volume 119 of *Proceedings of Machine Learning Research*, 2206–2216. Vienna, Austria: PMLR.
- Donnelly, J.; Barnett, A. J.; and Chen, C. 2022. Deformable ProtoPNet: An Interpretable Image Classifier Using Deformable Prototypes. In *IEEE/CVF Conference on Computer Vision and Pattern Recognition – CVPR 2022*, 10255–10265. New Orleans, LA, USA: IEEE.
- Ghiasi-Shirazi, K. 2019. Generalizing the Convolution Operator in Convolutional Neural Networks. *Neural Processing Letters*, 50(3): 2627–2646.
- Haasdonk, B.; and Keysers, D. 2002. Tangent distance kernels for support vector machines. In *Proceedings of the 16th International Conference on Pattern Recognition – ICPR 2002*, 864–868. Québec City, QC, Canada: IEEE.
- Hase, P.; Chen, C.; Li, O.; and Rudin, C. 2019. Interpretable Image Recognition with Hierarchical Prototypes. In Law, E.; and Vaughan, J. W., eds., *Proceedings of the Seventh AAAI Conference on Human Computation and Crowdsourcing, – HCOMP 2019*, 32–40. Stevenson, WA, USA: AAAI Press.
- Hastie, T.; Simard, P.; and Säckinger, E. 1995. Learning Prototype Models for Tangent Distance. In Tesauro, G.; Touretzky, D. S.; and Leen, T. K., eds., *Advances in Neural Information Processing Systems 7: Proceedings of the Neural Information Processing Systems Conference – NIPS 1994*, 999–1006. Denver, CO, USA: MIT Press.
- Hein, M.; Andriushchenko, M.; and Bitterwolf, J. 2019. Why ReLU networks yield high-confidence predictions far away from the training data and how to mitigate the problem. In *Proceedings of the 2019 IEEE/CVF Conference on Computer Vision and Pattern Recognition – CVPR 2019*, 41–50. Long Beach, CA, USA: IEEE.
- Hoffmann, A.; Fanconi, C.; Rade, R.; and Kohler, J. 2021. This Looks Like That... Does it? Shortcomings of Latent Space Prototype Interpretability in Deep Networks. *ICML 2021 Workshop on Theoretic Foundation, Criticism, and Application Trend of Explainable AI*.
- Hsu, A. S.; Horng, A.; Griffiths, T. L.; and Chater, N. 2017. When Absence of Evidence Is Evidence of Absence: Rational Inferences From Absent Data. *Cognitive Science*, 41(S5): 1155–1167.
- Kingma, D. P.; and Ba, J. 2015. Adam: A Method for Stochastic Optimization. In Bengio, Y.; and LeCun, Y., eds., *Proceedings of the 3rd International Conference on Learning Representations – ICLR 2015*. San Diego, CA, USA.
- Krause, J.; Stark, M.; Deng, J.; and Fei-Fei, L. 2013. 3D Object Representations for Fine-Grained Categorization. In *2013 IEEE International Conference on Computer Vision Workshops, ICCV Workshops 2013, Sydney, Australia, December 1-8, 2013*, 554–561. IEEE Computer Society.
- LeCun, Y.; Bottou, L.; Bengio, Y.; and Haffner, P. 1998. Gradient-based learning applied to document recognition. *Proceedings of the IEEE*, 86(11): 2278–2324.
- LeCun, Y.; Cortes, C.; and Burges, C. J. 1998. The MNIST database of handwritten digits. <http://yann.lecun.com/exdb/mnist/>.
- Liu, Z.; Mao, H.; Wu, C.; Feichtenhofer, C.; Darrell, T.; and Xie, S. 2022. A ConvNet for the 2020s. In *IEEE/CVF Conference on Computer Vision and Pattern Recognition – CVPR 2022*, 11966–11976. New Orleans, LA, USA: IEEE.
- Ma, C.; Donnelly, J.; Liu, W.; Vosoughi, S.; Rudin, C.; and Chen, C. 2024. Interpretable Image Classification with Adaptive Prototype-based Vision Transformers. In *arXiv:2410.20722*. Accepted at NeurIPS 2024.
- Marcinkevičs, R.; and Vogt, J. E. 2023. Interpretable and explainable machine learning: A methods-centric overview with concrete examples. *WIREs Data Mining and Knowledge Discovery*, 13(3): e1493.
- Mathiasen, A.; Hvilshøj, F.; Jørgensen, J. R.; Nasery, A.; and Mottin, D. 2020. What if Neural Networks had SVDs? In Larochelle, H.; Ranzato, M.; Hadsell, R.; Balcan, M.; and Lin, H., eds., *Advances in Neural Information Processing Systems 33: Proceedings of the Neural Information Processing Systems Conference – NeurIPS 2020*.
- Molnar, C. 2022. *Interpretable machine learning - A Guide for Making Black Box Models Explainable*. 2 edition.
- Nauta, M.; Schlötterer, J.; van Keulen, M.; and Seifert, C. 2023. PIP-Net: Patch-Based Intuitive Prototypes for Interpretable Image Classification. In *IEEE/CVF Conference on Computer Vision and Pattern Recognition – CVPR 2023*, 2744–2753. IEEE.
- Nauta, M.; van Bree, R.; and Seifert, C. 2021. Neural Prototype Trees for Interpretable Fine-grained Image Recognition. In *Proceedings of the 2021 IEEE/CVF Conference on Computer Vision and Pattern Recognition – CVPR 2021*, 14933–14943. Nashville, TN, USA: IEEE.
- Pach, M.; Rymarczyk, D.; Lewandowska, K.; Tabor, J.; and Zielinski, B. 2024. LucidPPN: Unambiguous Prototypical Parts Network for User-centric Interpretable Computer Vision. In *arXiv:2405.14331*.
- Parkhi, O. M.; Vedaldi, A.; Zisserman, A.; and Jawahar, C. V. 2012. Cats and dogs. In *Proceedings of the 2012 IEEE Computer Society Conference on Computer Vision and Pattern Recognition – CVPR 2012*, 3498–3505. Providence, RI, USA: IEEE.
- Pazzani, M. J.; Soltani, S.; Kaufman, R.; Qian, S.; and Hsiao, A. 2022. Expert-Informed, User-Centric Explanations for Machine Learning. In *Proceedings of the Thirty-Sixth AAAI Conference on Artificial Intelligence – AAAI 2022*, 12280–12286. AAAI Press.
- Ribeiro, M. T.; Singh, S.; and Guestrin, C. 2016. "Why

- Should I Trust You?": Explaining the Predictions of Any Classifier. In *Proceedings of the 22nd ACM SIGKDD International Conference on Knowledge Discovery and Data Mining*, 1135–1144. ACM.
- Rudin, C. 2019. Stop explaining black box machine learning models for high stakes decisions and use interpretable models instead. *Nature Machine Intelligence*, 1: 206–215.
- Rymarczyk, D.; Struski, L.; Górszczak, M.; Lewandowska, K.; Tabor, J.; and Zielinski, B. 2022. Interpretable Image Classification with Differentiable Prototypes Assignment. In Avidan, S.; Brostow, G. J.; Cissé, M.; Farinella, G. M.; and Hassner, T., eds., *Proceedings of the 17th European Conference on Computer Vision – ECCV 2022*, volume 13672 of the Lecture Notes in Computer Science, 351–368. Tel Aviv, Israel: Springer.
- Sacha, M.; Jura, B.; Rymarczyk, D.; Struski, L.; Tabor, J.; and Zielinski, B. 2024. Interpretability Benchmark for Evaluating Spatial Misalignment of Prototypical Parts Explanations. In Wooldridge, M. J.; Dy, J. G.; and Natarajan, S., eds., *Proceedings of the Thirty-Eighth Conference on Artificial Intelligence – AAAI 2024*, 21563–21573. Vancouver, Canada: AAAI Press.
- Saralajew, S.; Holdijk, L.; Rees, M.; Asan, E.; and Villmann, T. 2019. Classification-by-components: Probabilistic modeling of reasoning over a set of components. In Wallach, H.; Larochelle, H.; Beygelzimer, A.; d'Alché-Buc, F.; Fox, E.; and Garnett, R., eds., *Advances in Neural Information Processing Systems 32: Proceedings of the Neural Information Processing Systems Conference – NeurIPS 2019*, 2792–2803. Vancouver, BC, Canada: Curran Associates, Inc.
- Saralajew, S.; Holdijk, L.; and Villmann, T. 2020. Fast Adversarial Robustness Certification of Nearest Prototype Classifiers for Arbitrary Seminorms. In Larochelle, H.; Ranzato, M.; Hadsell, R.; Balcan, M.; and Lin, H., eds., *Advances in Neural Information Processing Systems 33: Proceedings of the Neural Information Processing Systems Conference – NeurIPS 2020*, 13635–13650. Curran Associates, Inc.
- Saralajew, S.; and Villmann, T. 2016. Adaptive tangent distances in generalized learning vector quantization for transformation and distortion invariant classification learning. In *Proceedings of the 2016 International Joint Conference on Neural Networks – IJCNN 2016*, 2672–2679. Vancouver, BC, Canada: IEEE.
- Sato, A.; and Yamada, K. 1996. Generalized Learning Vector Quantization. In Touretzky, D. S.; Mozer, M.; and Hasselmo, M. E., eds., *Advances in Neural Information Processing Systems 8: Proceedings of the Neural Information Processing Systems Conference – NIPS 1995*, 423–429. Denver, CO, USA: MIT Press.
- Seo, S.; and Obermayer, K. 2003. Soft Learning Vector Quantization. *Neural Computation*, 15(7): 1589–1604.
- van Amersfoort, J.; Smith, L.; Teh, Y. W.; and Gal, Y. 2020. Uncertainty Estimation Using a Single Deep Deterministic Neural Network. In *Proceedings of the 37th International Conference on Machine Learning – ICML 2020*, volume 119 of *Proceedings of Machine Learning Research*, 9690–9700. Vienna, Austria: PMLR.
- Villmann, T.; Bohnsack, A.; and Kaden, M. 2017. Can Learning Vector Quantization be an Alternative to SVM and Deep Learning? - Recent Trends and Advanced Variants of Learning Vector Quantization for Classification Learning. *Journal of Artificial Intelligence and Soft Computing Research*, 7(1): 65–81.
- Voráček, V.; and Hein, M. 2022. Provably Adversarially Robust Nearest Prototype Classifiers. In Chaudhuri, K.; Jegelka, S.; Song, L.; Szepesvári, C.; Niu, G.; and Sabato, S., eds., *Proceedings of the 39th International Conference on Machine Learning – ICML 2022*, volume 162 of the Proceedings of Machine Learning Research, 22361–22383. Baltimore, MD, USA: PMLR.
- Wah, C.; Branson, S.; Welinder, P.; Perona, P.; and Belongie, S. 2011. Caltech-UCSD Birds-200-2011 (CUB-200-2011). Technical Report CNS-TR-2011-001.
- Wang, J.; Liu, H.; Wang, X.; and Jing, L. 2021. Interpretable Image Recognition by Constructing Transparent Embedding Space. In *2021 IEEE/CVF International Conference on Computer Vision, ICCV 2021, Montreal, QC, Canada, October 10-17, 2021*, 875–884. IEEE.
- Wolf, T. N.; Bongratz, F.; Rickmann, A.; Pölsterl, S.; and Wachinger, C. 2024. Keep the Faith: Faithful Explanations in Convolutional Neural Networks for Case-Based Reasoning. In Wooldridge, M. J.; Dy, J. G.; and Natarajan, S., eds., *Proceedings of the Thirty-Eighth Conference on Artificial Intelligence – AAAI 2024*, 5921–5929. Vancouver, Canada: AAAI Press.

## A Derivation of the Tangent Distance and Extension to Restricted Versions

The tangent distance is a transformation-invariant measure. Instead of learning an individual prototype, it learns an affine subspace to model the data manifold of a given class (Haasdonk and Keyzers 2002; Hastie, Simard, and Säckinger 1995). Its effectiveness was demonstrated multiple times. Given an affine subspace that models the data and an input sample, the tangent distance is defined as the minimal Euclidean distance between the affine subspace and the input sample:

$$d_T(\mathbf{x}, S) = \min_{\theta \in \mathbb{R}^r} d_E(\mathbf{x}, \mathbf{w} + \mathbf{W}\theta),$$

where  $S = \{\mathbf{w} + \mathbf{W}\theta \mid \theta \in \mathbb{R}^r\}$  is an  $r$ -dimensional affine subspace with  $\mathbf{W}$  being an orthonormal basis (i. e.,  $\mathbf{W}^T \mathbf{W} = \mathbf{I}$ ). It can be shown that the minimizer  $\mathbf{w}^*(\mathbf{x})$  is given by

$$\mathbf{w}^*(\mathbf{x}) = \mathbf{w} + \mathbf{W}\mathbf{W}^T(\mathbf{x} - \mathbf{w}), \quad (11)$$

which is the best approximating element. Using this result, the tangent distance becomes

$$\begin{aligned} d_T(\mathbf{x}, S) &= \|\mathbf{x} - \mathbf{w} - \mathbf{W}\mathbf{W}^T(\mathbf{x} - \mathbf{w})\|_E \\ &= \|(\mathbf{I} - \mathbf{W}\mathbf{W}^T)(\mathbf{x} - \mathbf{w})\|_E. \end{aligned}$$

Note that  $\mathbf{I} - \mathbf{W}\mathbf{W}^T$  is an orthogonal projector and, hence, is idempotent, which implies

$$d_T(\mathbf{x}, S) = \sqrt{(\mathbf{x} - \mathbf{w})^T (\mathbf{I} - \mathbf{W}\mathbf{W}^T) (\mathbf{x} - \mathbf{w})}.$$

This equation can be used as a dissimilarity measure in classification learning frameworks where the affine subspace is learned from data (Saralajew and Villmann 2016). Moreover, this equation can be efficiently implemented and even generalized to sliding operations (similar to a convolution that uses the dot product) on parallel computing hardware. If the measure is used to learn the affine subspaces, it is important that the basis matrix is orthonormalized after each update step or that a proper encoding is applied. For instance, the former can be achieved by a polar decomposition via SVD and the latter by coding the matrices as Householder matrices (Mathiasen et al. 2020). After learning the affine subspaces,  $\mathbf{W}$  captures the invariant class dimensions, which are dimensions that are invariant with respect to class discrimination. Moreover, the vector  $\mathbf{w}$  represents a data point similar to an ordinary prototype, a point that represents the surrounding data as well as possible.

There are also extensions of this dissimilarity measure that constrain the affine subspace. For example, one can define a threshold  $\gamma > 0$  and modify Eq. (10) to

$$d_{CT}(\mathbf{x}, S) = \min_{\theta \in \mathbb{R}^r, \|\theta\|_E \leq \gamma} d_E(\mathbf{x}, \mathbf{w} + \mathbf{W}\theta),$$

which constrains the  $r$ -dimensional affine subspace to an  $r$ -dimensional hyperball. The solution for this distance is

$$d_{CT}(\mathbf{x}, S) = \sqrt{d_E^2(\mathbf{x}, \mathbf{w}^*(\mathbf{x})) + (\max\{0, d_E(\mathbf{w}, \mathbf{w}^*(\mathbf{x})) - \gamma\})^2}.$$

Like before, this measure can be efficiently implemented so that it is possible to learn these hyperballs from data, which are like affine subspaces that know the neighborhood they are approximating.

## B Derivation of the Robust Lower Bounds

In the following, we prove the presented theorems. For this, we prove a lemma that simplifies assumptions such as a class-independent temperature. Then, using the lemma, we prove Thm. 1. Later on, based on Thm. 1 and the proven lemma, we prove Thm. 2 and 3.

### B.1 Robustness lower bound for component-independent temperature and a specific incorrect class

**Lemma 4.** *The robustness of a correctly classified sample  $\mathbf{x}$  with class label  $y$  with respect to another class  $c'$  and temperature  $\sigma_k = \sigma$  for all components in the detection probability Eq. (5), where the distance is any distance  $d(\cdot, \cdot)$  induced by a norm  $\|\cdot\|$ , is lower bounded by*

$$\|\mathbf{e}^*\| \geq \sigma \ln \left( -\frac{B + \sqrt{B^2 - 4AC}}{2A} \right) > 0, \quad (12)$$

when  $A \neq 0$ , where

$$\begin{aligned} A &= ((\mathbf{r}_y - \mathbf{1}) \circ \mathbf{b}_y - \mathbf{r}_{c'} \circ \mathbf{b}_{c'})^T \mathbf{d}(\mathbf{x}), \\ B &= (\mathbf{1} - \mathbf{r}_y)^T \mathbf{b}_y - (\mathbf{1} - \mathbf{r}_{c'})^T \mathbf{b}_{c'}, \\ C &= (\mathbf{r}_y \circ \mathbf{b}_y - (\mathbf{r}_{c'} - \mathbf{1}) \circ \mathbf{b}_{c'})^T \mathbf{d}(\mathbf{x}). \end{aligned}$$

*Proof.* To derive this bound, we perform the following steps:

1. We lower bound the probability gap

$$p_y(\mathbf{x} + \boldsymbol{\varepsilon}) - p_{c'}(\mathbf{x} + \boldsymbol{\varepsilon}) > 0 \quad (13)$$

for an arbitrary  $\boldsymbol{\varepsilon} \in \mathbb{R}^n$  by using the triangle inequality.

2. We show that the derived lower bound for the probability gap is (strictly) monotonic decreasing with respect to increasing  $\|\boldsymbol{\varepsilon}\|$ .
3. We show that the derived lower bound has one root. This root is a lower bound for the maximum perturbation  $\|\boldsymbol{\varepsilon}^*\|$  as the increase of  $\|\boldsymbol{\varepsilon}\|$  beyond this value results in a negative lower bound of the probability gap (because of the monotonic decreasing behavior) and, hence, potential misclassification.

**Lower bound the probability gap.** We use the triangle inequality and conclude that

$$\exp\left(-\frac{d(\mathbf{x} + \boldsymbol{\varepsilon}, \mathbf{w}_k)}{\sigma}\right) \geq \exp\left(-\frac{d(\mathbf{x}, \mathbf{w}_k)}{\sigma}\right) \underbrace{\exp\left(-\frac{\|\boldsymbol{\varepsilon}\|}{\sigma}\right)}_{=:\exp(-z)}, \quad (14)$$

where  $d(\mathbf{x} + \boldsymbol{\varepsilon}, \mathbf{w}_k) \leq d(\mathbf{x} + \boldsymbol{\varepsilon}, \mathbf{x}) + d(\mathbf{x}, \mathbf{w}_k) = \|\boldsymbol{\varepsilon}\| + d(\mathbf{x}, \mathbf{w}_k)$  and  $z = \frac{\|\boldsymbol{\varepsilon}\|}{\sigma}$  has been used. Similarly, we conclude that

$$\exp\left(-\frac{d(\mathbf{x} + \boldsymbol{\varepsilon}, \mathbf{w}_k)}{\sigma}\right) \leq \exp\left(-\frac{d(\mathbf{x}, \mathbf{w}_k)}{\sigma}\right) \underbrace{\exp\left(\frac{\|\boldsymbol{\varepsilon}\|}{\sigma}\right)}_{=\exp(z)} \quad (15)$$

by using  $d(\mathbf{x} + \boldsymbol{\varepsilon}, \mathbf{w}_k) \geq -d(\mathbf{x} + \boldsymbol{\varepsilon}, \mathbf{x}) + d(\mathbf{x}, \mathbf{w}_k) = -\|\boldsymbol{\varepsilon}\| + d(\mathbf{x}, \mathbf{w}_k)$ .

Now, we use these results and lower bound the probability gap Eq. (13). In the first step, we apply the lower and upper bound for the disturbed detection probability, see Eq. (14) and Eq. (15), respectively, to lower bound the output probability Eq. (4) for the correct class:

$$\begin{aligned} p_y(\mathbf{x} + \boldsymbol{\varepsilon}) &= (\mathbf{r}_y \circ \mathbf{d}(\mathbf{x} + \boldsymbol{\varepsilon}) + (\mathbf{1} - \mathbf{r}_y) \circ (\mathbf{1} - \mathbf{d}(\mathbf{x} + \boldsymbol{\varepsilon})))^T \mathbf{b}_y \\ &\geq (\mathbf{r}_y \circ \mathbf{d}(\mathbf{x}) \exp(-z) + (\mathbf{1} - \mathbf{r}_y) \circ (\mathbf{1} - \mathbf{d}(\mathbf{x}) \exp(z)))^T \mathbf{b}_y \\ &= (\mathbf{r}_y \circ \mathbf{d}(\mathbf{x}) \exp(-z) + \mathbf{1} - \mathbf{d}(\mathbf{x}) \exp(z) - \mathbf{r}_y + \mathbf{r}_y \circ \mathbf{d}(\mathbf{x}) \exp(z))^T \mathbf{b}_y \\ &= (\mathbf{r}_y \circ \mathbf{b}_y)^T \mathbf{d}(\mathbf{x}) \exp(-z) + (\mathbf{1} - \mathbf{r}_y)^T \mathbf{b}_y + ((\mathbf{r}_y - \mathbf{1}) \circ \mathbf{b}_y)^T \mathbf{d}(\mathbf{x}) \exp(z). \end{aligned} \quad (16)$$

Note that this bound holds with equality (becomes the undisturbed probability gap) if  $z = 0$ . Next, we upper bound the output probability for the incorrect class:

$$\begin{aligned} p_{c'}(\mathbf{x} + \boldsymbol{\varepsilon}) &= (\mathbf{r}_{c'} \circ \mathbf{d}(\mathbf{x} + \boldsymbol{\varepsilon}) + (\mathbf{1} - \mathbf{r}_{c'}) \circ (\mathbf{1} - \mathbf{d}(\mathbf{x} + \boldsymbol{\varepsilon})))^T \mathbf{b}_{c'} \\ &\leq (\mathbf{r}_{c'} \circ \mathbf{d}(\mathbf{x}) \exp(z) + (\mathbf{1} - \mathbf{r}_{c'}) \circ (\mathbf{1} - \mathbf{d}(\mathbf{x}) \exp(-z)))^T \mathbf{b}_{c'} \\ &= (\mathbf{r}_{c'} \circ \mathbf{b}_{c'})^T \mathbf{d}(\mathbf{x}) \exp(z) + (\mathbf{1} - \mathbf{r}_{c'})^T \mathbf{b}_{c'} + ((\mathbf{r}_{c'} - \mathbf{1}) \circ \mathbf{b}_{c'})^T \mathbf{d}(\mathbf{x}) \exp(-z). \end{aligned} \quad (17)$$

Again, note that this bound holds with equality if  $z = 0$ . Combining the two results yields

$$p_y(\mathbf{x} + \boldsymbol{\varepsilon}) - p_{c'}(\mathbf{x} + \boldsymbol{\varepsilon}) \geq C \exp(-z) + A \exp(z) + B =: f(z),$$

which holds with equality if  $z = 0$  and whereby

$$\begin{aligned} A &= ((\mathbf{r}_y - \mathbf{1}) \circ \mathbf{b}_y - \mathbf{r}_{c'} \circ \mathbf{b}_{c'})^T \mathbf{d}(\mathbf{x}), \\ B &= (\mathbf{1} - \mathbf{r}_y)^T \mathbf{b}_y - (\mathbf{1} - \mathbf{r}_{c'})^T \mathbf{b}_{c'}, \\ C &= (\mathbf{r}_y \circ \mathbf{b}_y - (\mathbf{r}_{c'} - \mathbf{1}) \circ \mathbf{b}_{c'})^T \mathbf{d}(\mathbf{x}). \end{aligned}$$

**The lower bound is monotonic decreasing.** Next, we show that the function  $f$  is monotonic decreasing. Assume  $z_1 < z_2$  and show that  $f(z_1) \geq f(z_2)$ :

$$\begin{aligned} C \exp(-z_1) + A \exp(z_1) &\geq C \exp(-z_2) + A \exp(z_2), \\ C \underbrace{(\exp(-z_1) - \exp(-z_2))}_{>0} + A \underbrace{(\exp(z_1) - \exp(z_2))}_{<0} &\geq 0. \end{aligned}$$

Considering the coefficient  $A$ , we can conclude that it is negative:

$$A = \left( \underbrace{(\mathbf{r}_y - \mathbf{1}) \circ \mathbf{b}_y}_{\in [-1, 0]^K} - \underbrace{\mathbf{r}_{c'} \circ \mathbf{b}_{c'}}_{\in [0, 1]^K} \right)^T \underbrace{\mathbf{d}(\mathbf{x})}_{\in [0, 1]^K} \leq 0.$$

Similarly, we can conclude that the coefficient  $B \in [-1, 1]$  and  $C \geq 0$ . Consequently, this implies that the function is monotonic decreasing with respect to  $z$  and even strictly monotonic decreasing if  $C$  or  $A$  is unequal zero.

**Computing the root.** Now, we want to compute a solution  $z_0 \in \mathbb{R}^+$  such that  $f(z_0) = 0$ , which means finding  $z_0$  for which the lower bound of the probability gap is zero. This also means that for points  $z < z_0$  (smaller perturbations) all perturbations will not lead to a change of the class assignment as  $f(z) > 0$  (concluded from the decreasing monotonic behavior). Similarly, for points above the root  $z > z_0$  the lower bound will be negative ( $f(z) < 0$ ) so that it cannot be guaranteed that there is no misclassification under a perturbation of strength  $z$ .

To compute the root, we solve the equation

$$C \exp(-z) + A \exp(z) + B = 0 \quad (18)$$

by multiplying with  $\exp(z)$  and substituting  $\exp(z)$  with  $\tilde{z}$ . This leads to

$$C + A\tilde{z}^2 + B\tilde{z} = 0.$$

The solution for this quadratic equation is

$$\tilde{z}_{1,2} = -\frac{B}{2A} \pm \frac{1}{2|A|} \sqrt{B^2 - 4AC}. \quad (19)$$

Note that this proof applies only to  $A \neq 0$ ; we discuss the case  $A = 0$  after this proof. Considering that the coefficient  $A$  is negative, we can conclude that

$$\tilde{z}_{1,2} = \frac{B \pm \sqrt{B^2 - 4AC}}{2|A|}.$$

Moreover,  $B \in [-1, 1]$  and  $C \geq 0$  implies that

$$|B| \leq \sqrt{B^2 - 4AC}, \quad (20)$$

and, further, that

$$\tilde{z}_1 = \frac{B + \sqrt{B^2 - 4AC}}{2|A|} \geq 0$$

is the potential solution because  $\tilde{z}$  must be positive to be a valid solution for  $\exp(z)$ . Additionally, we have to show that  $\tilde{z}_1 > 1$  because  $z$  must be positive. For this, we first show that

$$\sqrt{B^2 - 4AC} + (2|A| - B) > 0. \quad (21)$$

This can be shown through the following steps using the result from Eq. (20):

$$\begin{aligned} & \overbrace{\frac{B - \sqrt{B^2 - 4AC}}{2|A|}}^{\leq 0} < 1, \\ & -B + \sqrt{B^2 - 4AC} > -2|A|, \\ & \sqrt{B^2 - 4AC} + (2|A| - B) > 0. \end{aligned}$$

Now we show that  $\tilde{z}_1 > 1$  by using the fact that  $A + B + C = p_y(\mathbf{x}) - p_{c'}(\mathbf{x}) > 0$ :

$$\begin{aligned} 0 &< |A| (p_y(\mathbf{x}) - p_{c'}(\mathbf{x})) \\ &= |A| (C + B + A) \\ &= -AC + |A|B - |A|^2. \end{aligned} \quad (22)$$

We multiply by 4 and add the term  $B^2$  on both sides:

$$0 < (B^2 - 4AC) - (4|A|^2 - 4|A|B + B^2).$$

Finally, we recognize the structure of  $(x-y)(x+y) = x^2 - y^2$  and cancel  $x+y$  by using Eq. (21), which completes the proof:

$$\begin{aligned} 0 &< (B^2 - 4AC) - (4|A|^2 - 4|A|B + B^2), \\ 0 &< \left(\sqrt{B^2 - 4AC} + (2|A| - B)\right) \left(\sqrt{B^2 - 4AC} - (2|A| - B)\right), \\ 0 &< \sqrt{B^2 - 4AC} - (2|A| - B), \\ 1 &< \frac{B + \sqrt{B^2 - 4AC}}{2|A|} = \tilde{z}_1. \end{aligned}$$

In summary, the solution for the *lower bound of disturbed probability gap* is

$$\|\varepsilon_0\| = \sigma \ln \left( -\frac{B + \sqrt{B^2 - 4AC}}{2A} \right) > 0. \quad (23)$$

Because this solution was computed for the lower bound of the probability gap, the robustness  $\|\varepsilon^*\|$  of a correctly classified sample  $\mathbf{x}$  with class label  $y$  with respect to another class is lower bounded by

$$\|\varepsilon^*\| \geq \sigma \ln \left( -\frac{B + \sqrt{B^2 - 4AC}}{2A} \right) > 0. \quad (24)$$

□

The previous lemma proves the robustness bound for when  $A \neq 0$ . This is not a restriction as an even simpler result can be obtained for the special case: If  $A = 0$ , Eq. (18) simplifies to

$$\exp(-z) = -\frac{B}{C}.$$

Taking into account that  $A = 0$  and that  $\mathbf{d}(\mathbf{x}) \neq \mathbf{0}$  for all  $\mathbf{x} \in \mathbb{R}^n$ , this implies that

$$-\mathbf{r}_{c'} \circ \mathbf{b}_{c'} = (\mathbf{1} - \mathbf{r}_y) \circ \mathbf{b}_y.$$

Using this result,  $C$  simplifies to

$$C = (\mathbf{b}_y + \mathbf{b}_{c'})^T \mathbf{d}(\mathbf{x}) \geq 0$$

and  $B$  to

$$B = -\mathbf{1}^T \mathbf{b}_{c'} = -1,$$

since  $\mathbf{b}_{c'}$  is a probability vector. Moreover,  $A + B + C > 0$  implies that

$$-\frac{B}{C} < 1.$$

Further, by substituting  $B$  and  $C$  we get

$$-\frac{B}{C} = \frac{1}{(\mathbf{b}_y + \mathbf{b}_{c'})^T \mathbf{d}(\mathbf{x})} > 0$$

so that we conclude

$$-\frac{B}{C} \in (0, 1)$$

Consequently, the solution  $z = -\ln\left(-\frac{B}{C}\right)$  is positive and valid and we get

$$\|\varepsilon^*\| \geq \sigma \ln \left( \mathbf{b}_y^T \mathbf{d}(\mathbf{x}) + \mathbf{b}_{c'}^T \mathbf{d}(\mathbf{x}) \right) > 0.$$

It must be noted that we assumed  $C = (\mathbf{b}_y + \mathbf{b}_{c'})^T \mathbf{d}(\mathbf{x}) \neq 0$ , which is valid since  $\mathbf{d}(\mathbf{x}) \neq \mathbf{0}$  and  $\mathbf{b}_y + \mathbf{b}_{c'} \neq \mathbf{0}$ . In practice, when we used the bound of Lem. 4 for robustness evaluations or model training, we never observed the special case of  $A = 0$ . Hence, we will not consider this special case for the following proofs. But we emphasize that all results can be extended for this special case so that focusing on  $A \neq 0$  is not a restriction.

In case of an incorrect classification, Eq. (22) changes to be less than zero as  $A + B + C < 0$ . Then, this leads to  $\tilde{z}_1 < 1$  so that the expression Eq. (24) becomes negative:

$$\sigma \ln \left( -\frac{B + \sqrt{B^2 - 4AC}}{2A} \right) < 0.$$

Hence, the sign of this expression follows the sign of the probability gap. Consequently, this expression can be used to formulate a loss that optimizes for robustness and correct classifications.

## B.2 Proof of Thm. 1

We now prove Thm. 1 by using Lem. 4. For completeness we restate the theorem:

**Theorem.** *The robustness of a correctly classified sample  $\mathbf{x}$  with class label  $y$  is lower bounded by*

$$\|\boldsymbol{\varepsilon}^*\| \geq \underbrace{\kappa \min_{c' \neq y} \left( \ln \left( -\frac{B_{c'} + \sqrt{B_{c'}^2 - 4A_{c'}C_{c'}}}{2A_{c'}} \right) \right)}_{=: \delta} > 0,$$

when  $A_{c'} \neq 0$ , where

$$\begin{aligned} A_{c'} &= ((\mathbf{r}_y - \mathbf{1}) \circ \mathbf{b}_y - \mathbf{r}_{c'} \circ \mathbf{b}_{c'})^T \mathbf{d}(\mathbf{x}), \\ B_{c'} &= (\mathbf{1} - \mathbf{r}_y)^T \mathbf{b}_y - (\mathbf{1} - \mathbf{r}_{c'})^T \mathbf{b}_{c'}, \\ C_{c'} &= (\mathbf{r}_y \circ \mathbf{b}_y - (\mathbf{r}_{c'} - \mathbf{1}) \circ \mathbf{b}_{c'})^T \mathbf{d}(\mathbf{x}), \end{aligned}$$

and  $\kappa = \sigma_{min} = \min_k \sigma_k$ .

*Proof.* The proof follows the technique used to prove Lem. 4 with the following changes: To account for a component-wise  $\sigma$ , we lower (upper) bound Eq. (14) and Eq. (15) again, respectively,

$$\exp\left(-\frac{d(\mathbf{x} + \boldsymbol{\varepsilon}, \mathbf{w}_k)}{\sigma_k}\right) \geq \exp\left(-\frac{d(\mathbf{x}, \mathbf{w}_k)}{\sigma_k}\right) \exp\left(-\frac{\|\boldsymbol{\varepsilon}\|}{\sigma_k}\right) \quad (25)$$

$$\geq \exp\left(-\frac{d(\mathbf{x}, \mathbf{w}_k)}{\sigma_k}\right) \exp\left(-\frac{\|\boldsymbol{\varepsilon}\|}{\sigma_{min}}\right), \quad (26)$$

$$\exp\left(-\frac{d(\mathbf{x} + \boldsymbol{\varepsilon}, \mathbf{w}_k)}{\sigma_k}\right) \leq \exp\left(-\frac{d(\mathbf{x}, \mathbf{w}_k)}{\sigma_k}\right) \exp\left(\frac{\|\boldsymbol{\varepsilon}\|}{\sigma_k}\right) \quad (27)$$

$$\leq \exp\left(-\frac{d(\mathbf{x}, \mathbf{w}_k)}{\sigma_k}\right) \exp\left(\frac{\|\boldsymbol{\varepsilon}\|}{\sigma_{min}}\right), \quad (28)$$

where  $\sigma_k$  is the component-wise temperature, and  $\sigma_{min} = \min\{\sigma_1, \dots, \sigma_K\}$ . Consequently, the lower bound for the correct class becomes

$$p_y(\mathbf{x} + \boldsymbol{\varepsilon}) \geq (\mathbf{r}_y \circ \mathbf{b}_y)^T \mathbf{d}(\mathbf{x}) \exp(-z_{min}) + (\mathbf{1} - \mathbf{r}_y)^T \mathbf{b}_y + ((\mathbf{r}_y - \mathbf{1}) \circ \mathbf{b}_y)^T \mathbf{d}(\mathbf{x}) \exp(z_{min}), \quad (29)$$

and the upper bound of the output probability for an incorrect class becomes

$$p_{c'}(\mathbf{x} + \boldsymbol{\varepsilon}) \leq (\mathbf{r}_{c'} \circ \mathbf{b}_{c'})^T \mathbf{d}(\mathbf{x}) \exp(z_{min}) + (\mathbf{1} - \mathbf{r}_{c'})^T \mathbf{b}_{c'} + ((\mathbf{r}_{c'} - \mathbf{1}) \circ \mathbf{b}_{c'})^T \mathbf{d}(\mathbf{x}) \exp(-z_{min}), \quad (30)$$

where  $z_{min} = \frac{\|\boldsymbol{\varepsilon}\|}{\sigma_{min}}$ .

Next, we assume that  $c'$  is any class label of an incorrect class. Following the steps from Lem. 4, we get the solution

$$\|\boldsymbol{\varepsilon}^*\| \geq \sigma_{min} \ln \left( -\frac{B + \sqrt{B^2 - 4AC}}{2A} \right) > 0. \quad (31)$$

Since we search for the smallest perturbation  $\|\boldsymbol{\varepsilon}\|$  that changes the prediction, we have to compute the bound for each class  $c' \neq y$  and have to pick the minimum, which completes the proof.  $\square$

In case multiple reasoning vectors per class are used,  $\mathbf{r}_c$  and  $\mathbf{b}_c$  become matrices containing the reasoning probability vectors  $\mathbf{r}_{c,i}$  and  $\mathbf{b}_{c,i}$  where  $i$  is the index. In this case, the classifier takes the maximum probability per class

$$p_c(\mathbf{x}) = \max_i p_{c,i}(\mathbf{x}),$$

and in Eq. (8) the maximum must be computed:

$$\|\boldsymbol{\varepsilon}^*\| \geq \kappa \min_{c' \neq y} \max_i \left( \ln \left( -\frac{B_{c',i} + \sqrt{B_{c',i}^2 - 4A_{c',i}C_{c',i}}}{2A_{c',i}} \right) \right) > 0.$$

### B.3 Proof of Thm. 2

We now prove Thm. 2 by extending the proof of Thm. 1. For completeness we restate the theorem:

**Theorem 5.** *If we use the standard RBF kernel (squared norm), then Eq. (8) becomes  $\|\varepsilon^*\| \geq -\frac{\beta}{3} + \sqrt{\frac{\beta^2}{9} + \delta} > 0$  with  $\kappa = \frac{\sigma_{min}}{3}$  and  $\beta = \max_k d(\mathbf{x}, \mathbf{w}_k)$ .*

The theorem states that the derived bound also holds for the frequently used squared exponential kernel (Gaussian RBF), which implicitly projects data into an infinite-dimensional space. In principle, any squared distance induced by a norm can be used.

*Proof.* The proof follows the technique used to prove Thm. 1 with the following changes: We modify the initial lower bounds of the distances. In Lem. 4, we used

$$d(\mathbf{x} + \varepsilon, \mathbf{w}_k) \leq \|\varepsilon\| + d(\mathbf{x}, \mathbf{w}_k)$$

to derive the result. If we square this inequality, we get

$$d^2(\mathbf{x} + \varepsilon, \mathbf{w}_k) \leq \|\varepsilon\|^2 + d^2(\mathbf{x}, \mathbf{w}_k) + 2\|\varepsilon\|d(\mathbf{x}, \mathbf{w}_k).$$

Among all  $d(\mathbf{x}, \mathbf{w}_k)$  there exists a maximum  $\beta = \max_k d(\mathbf{x}, \mathbf{w}_k)$ . Using this result, we get

$$d^2(\mathbf{x} + \varepsilon, \mathbf{w}_k) \leq \left( \|\varepsilon\|^2 + 2\|\varepsilon\|\beta \right) + d^2(\mathbf{x}, \mathbf{w}_k)$$

and we further we relax the bound to

$$d^2(\mathbf{x} + \varepsilon, \mathbf{w}_k) \leq \left( 3\|\varepsilon\|^2 + 2\|\varepsilon\|\beta \right) + d^2(\mathbf{x}, \mathbf{w}_k).$$

With this, we get for the lower bound of the detection probability Eq. (14)

$$\exp\left(-\frac{d^2(\mathbf{x} + \varepsilon, \mathbf{w}_k)}{\sigma}\right) \geq \exp\left(-\frac{d^2(\mathbf{x}, \mathbf{w}_k)}{\sigma}\right) \underbrace{\exp\left(-\frac{3\|\varepsilon\|^2 + 2\beta\|\varepsilon\|}{\sigma}\right)}_{=:\exp(-z)}.$$

Similarly, we can derive the following result for the squared triangle inequality of  $d(\mathbf{x}, \mathbf{w}_k) \leq \|\varepsilon\| + d(\mathbf{x} + \varepsilon, \mathbf{w}_k)$ :

$$\begin{aligned} d^2(\mathbf{x}, \mathbf{w}_k) &\leq \|\varepsilon\|^2 + d^2(\mathbf{x} + \varepsilon, \mathbf{w}_k) + 2\|\varepsilon\|d(\mathbf{x} + \varepsilon, \mathbf{w}_k) \\ &\leq \|\varepsilon\|^2 + d^2(\mathbf{x} + \varepsilon, \mathbf{w}_k) + 2\|\varepsilon\|(\|\varepsilon\| + d(\mathbf{x}, \mathbf{w}_k)) \\ &= \|\varepsilon\|^2 + d^2(\mathbf{x} + \varepsilon, \mathbf{w}_k) + 2\|\varepsilon\|^2 + 2\|\varepsilon\|d(\mathbf{x}, \mathbf{w}_k) \\ &= \|\varepsilon\|^2 + d^2(\mathbf{x} + \varepsilon, \mathbf{w}_k) + 2\|\varepsilon\|^2 + 2\beta\|\varepsilon\| \\ &= \left( 3\|\varepsilon\|^2 + 2\beta\|\varepsilon\| \right) + d^2(\mathbf{x} + \varepsilon, \mathbf{w}_k). \end{aligned}$$

This implies that

$$d^2(\mathbf{x} + \varepsilon, \mathbf{w}_k) \geq -\left( 3\|\varepsilon\|^2 + 2\beta\|\varepsilon\| \right) + d^2(\mathbf{x}, \mathbf{w}_k)$$

and for the upper bound of the detection probability Eq. (15)

$$\exp\left(-\frac{d^2(\mathbf{x} + \varepsilon, \mathbf{w}_k)}{\sigma}\right) \leq \exp\left(-\frac{d^2(\mathbf{x}, \mathbf{w}_k)}{\sigma}\right) \underbrace{\exp\left(\frac{3\|\varepsilon\|^2 + 2\beta\|\varepsilon\|}{\sigma}\right)}_{=\exp(z)}.$$

By using the results of Lem. 4, we get for the root Eq. (23)

$$3\|\varepsilon'_0\|^2 + 2\beta\|\varepsilon'_0\| = \sigma \ln\left(-\frac{B + \sqrt{B^2 - 4AC}}{2A}\right) = \|\varepsilon_0\| > 0.$$

If we solve this equation for  $\|\varepsilon'_0\|$ , we get

$$\|\varepsilon'_0\| = -\frac{\beta}{3} + \sqrt{\frac{\beta^2}{9} + \frac{1}{3}\|\varepsilon_0\|} > 0 \quad (32)$$

for the valid solution as the negative part would lead to a negative  $\|\varepsilon'_0\|$ . By following the additional proof steps of Thm. 1, we get the result.  $\square$



It should be noted, that this result only considers correctly classified samples. For incorrectly classified samples, the expression to determine  $\|\varepsilon_0\|$  (which means  $\delta$ ) becomes negative; hence, Eq. (32) cannot be computed since the quadratic equation could have no roots. Consequently, Eq. (32) cannot be used to formulate a closed-form loss function for correctly and incorrectly classified samples. However, for incorrectly classified samples, it is sufficient to optimize  $\delta$  (i. e., Eq. (24)) and optimize Eq. (32) for correctly classified samples. The joint formulation takes the form:

$$\begin{cases} -\frac{\beta}{3} + \sqrt{\frac{\beta^2}{9} + \delta} & \text{if } p_y(\mathbf{x}) - p_{c'}(\mathbf{x}) > 0, \\ \lambda \cdot \delta & \text{otherwise,} \end{cases} \quad (33)$$

where  $\lambda > 0$  is a regularization factor to balance the two differently scaled loss terms.

For Gaussian kernel RBF networks, Eq. (32) can be simplified by Eq. (9). This presents the first result about robustness optimization of Gaussian kernel RBF networks. In general, the term  $\beta$  has a minor contribution to the network optimization. Thus, similar to the non-squared case, it is sufficient to only optimize  $\delta$ . However, to obtain a precise robustness value via a margin loss formulation, Eq. (32) must be optimized.

#### B.4 Proof of Thm. 3

We now prove Thm. 3 by extending the proof of Thm. 1. For completeness we restate the theorem:

**Theorem.** *If we use the tangent distance in the RBF of Eq. (5), then Eq. (8) holds with  $\kappa = \frac{1}{2}\sigma_{min}$  and  $\|\cdot\|$  being the Euclidean norm.*

See Appx. A for information about the tangent distance.

*Proof.* The proof follows the technique used to prove Thm. 1 with the following changes: We modify the initial lower bounds of the distances. The goal is to derive a lower bound for

$$d_T(\mathbf{x} + \varepsilon, S) = d_E(\mathbf{x} + \varepsilon, \mathbf{w}^*(\mathbf{x} + \varepsilon)),$$

where  $\mathbf{w}^*(\mathbf{x})$  is the best approximating element with respect to  $\mathbf{x}$ , see Eq. (11). Similar to before (see Eq. (14)) we apply the triangle inequality to derive

$$d_E(\mathbf{x} + \varepsilon, \mathbf{w}^*(\mathbf{x} + \varepsilon)) \leq \|\varepsilon\|_E + d_E(\mathbf{x}, \mathbf{w}^*(\mathbf{x} + \varepsilon)).$$

Now, we upper bound  $d_E(\mathbf{x}, \mathbf{w}^*(\mathbf{x} + \varepsilon))$  by applying the triangle inequality again:

$$\begin{aligned} d_E(\mathbf{x}, \mathbf{w}^*(\mathbf{x} + \varepsilon)) &\leq d_E(\mathbf{x}, \mathbf{w}^*(\mathbf{x})) + d_E(\mathbf{w}^*(\mathbf{x}), \mathbf{w}^*(\mathbf{x} + \varepsilon)) \\ &= d_T(\mathbf{x}, S) + d_E(\mathbf{w}^*(\mathbf{x}), \mathbf{w}^*(\mathbf{x} + \varepsilon)). \end{aligned}$$

The expression  $d_E(\mathbf{w}^*(\mathbf{x}), \mathbf{w}^*(\mathbf{x} + \varepsilon))$  can be upper bounded by  $\|\varepsilon\|_E$ :

$$\begin{aligned} d_E(\mathbf{w}^*(\mathbf{x}), \mathbf{w}^*(\mathbf{x} + \varepsilon)) &= d_E(\mathbf{w} + \mathbf{W}\mathbf{W}^T(\mathbf{x} - \mathbf{w}), \mathbf{w} + \mathbf{W}\mathbf{W}^T(\mathbf{x} + \varepsilon - \mathbf{w})) \\ &= \|\mathbf{w} + \mathbf{W}\mathbf{W}^T(\mathbf{x} - \mathbf{w}) - \mathbf{w} - \mathbf{W}\mathbf{W}^T(\mathbf{x} + \varepsilon - \mathbf{w})\|_E \\ &= \|\mathbf{W}\mathbf{W}^T\varepsilon\|_E \\ &= \sqrt{\varepsilon^T \underbrace{\mathbf{W}\mathbf{W}^T\mathbf{W}\mathbf{W}^T}_{\mathbf{I}} \varepsilon} \\ &= \sqrt{\varepsilon^T \mathbf{W}\mathbf{W}^T \varepsilon} \\ &= \|\mathbf{W}^T\varepsilon\|_E. \end{aligned}$$

Next, we use the fact that the Euclidean norm is compatible with the spectral norm and that the spectral norm of  $\mathbf{W}^T$  is 1 (because of the orthonormal basis assumption):

$$d_E(\mathbf{w}^*(\mathbf{x}), \mathbf{w}^*(\mathbf{x} + \varepsilon)) = \|\mathbf{W}^T\varepsilon\|_E \leq \underbrace{\|\mathbf{W}^T\|_E}_{=1} \|\varepsilon\|_E = \|\varepsilon\|_E.$$

Finally, combining the results we get

$$d_T(\mathbf{x} + \varepsilon, S) \leq 2\|\varepsilon\|_E + d_T(\mathbf{x}, S).$$

Similarly, we can derive

$$d_T(\mathbf{x} + \varepsilon, S) \geq -2\|\varepsilon\|_E + d_T(\mathbf{x}, S).$$

Using these two results in Eq. (14) and Eq. (15), we conclude that the robustness lower bound for the tangent distance is given by

$$\|\varepsilon^*\|_E \geq \frac{\sigma_{min}}{2} \min_{c' \neq y} \left( \ln \left( -\frac{B_{c'} + \sqrt{B_{c'}^2 - 4A_{c'}C_{c'}}}{2A_{c'}} \right) \right) > 0.$$

□

Note that compared to Thm. 1, we leverage the triangle inequality multiple times over the same expression. Hence, it must be expected that the derived lower bound is not as tight as for Thm. 1. The same applies to Thm. 2.

If we combine this result with Thm. 2, we can conclude that we have to divide the result of Thm. 2 by 2. This result can be obtained by substituting  $2\|\varepsilon\|_E$  with a new variable and by following the proof steps of Thm. 2.

## C Further Theoretical Results

**A motivating example for negative reasoning.** In general, negative reasoning as the retrieval of evidence from absent features is not only supported by results from cognitive science (Hsu et al. 2017) but can also be motivated by a thought experiment: Assume a fine-grained multi-class classification problem. Between two close classes,  $A$  and  $B$ , only the presence of one particular base feature discriminates between the two classes (present for  $A$  and not present for  $B$ ). Further, both classes are supported by  $N$  detectable base features. If only positive reasoning is allowed, classes  $A$  and  $B$  will be supported by, at most,  $N + 1$  and  $N$  features, respectively. If all features contribute equally to the class evidence, the absence of a base feature has a higher impact on class  $B$  than it has on class  $A$ . Consequently, how features could contribute to the class evidence is not balanced. If negative reasoning were used, the problem would be fixed since both classes would be supported by  $N + 1$  features (presence or absence contributes).

**When is  $p_c(\mathbf{x}) = 0$  or  $p_c(\mathbf{x}) = 1$ ?** Only if the reasoning and the detection probabilities become crisp (binary) vectors. This can be easily shown by considering the probability tree diagram. Understanding when the “optimal” probability outputs can be generated is important. It also implies that the classification output cannot be more discriminating than the detection probability function. Hence, if one wants to improve the classification power of the model, the discrimination power of the detection probability function must be improved.

**How do we initialize the  $\sigma_k$  in Eq. (5) such that the gradients do not vanish during training?** If  $\sigma_k$  is not chosen correctly, the network can be difficult to train because of vanishing gradients. To avoid this, we propose the following initialization strategy: The idea is to compute how much the distances between data points vary and to select  $\sigma_k$  such that this value is mapped to a small probability. Assume that the mean distance is denoted by *mean* and the standard deviation of the distances is denoted by *std*, then  $\sigma_k$  can be initialized by

$$\sigma = -\frac{\text{mean} + \text{std}}{\ln(p_0)}, \quad (34)$$

whereby  $p_0$  is a defined lower bound for the expected detection similarity (e. g.,  $p_0 = 0.01$ ). Moreover, the concepts Ghiasi-Shirazi (2019) developed can also be applied.

**Relation to Generalized Learning Vector Quantization (Sato and Yamada 1996).** It turns out that our CBC is equivalent to GLVQ under certain circumstances. More precisely, if the reasoning becomes crisp and is only driven by positive reasoning, it constitutes a one-hot vector coding of class responsibility such that the CBC components realize class-specific GLVQ prototypes. In this situation, the CBC optimization of the probability gap yields the optimization of a scaled hypothesis margin in GLVQ:

$$\text{HypothesisMargin}(\mathbf{x}) = \frac{1}{2} \left( d_E(\mathbf{x}, \mathbf{w}_{k_{c'}}) - d_E(\mathbf{x}, \mathbf{w}_{k_y}) \right),$$

where  $\mathbf{w}_{k_{c'}}$  is the best matching prototype of an incorrect class, and  $\mathbf{w}_{k_y}$  is the best matching prototype of the correct class. Consequently, the optimization of the probability gap optimizes for robustness. At the same time, our derived robust loss formulation Eq. (9) simplifies to a scaled hypothesis margin as well. Assume that  $k_y$  is the one-hot index of  $\mathbf{v}_y$  and  $k_{c'}$  is the index of  $\mathbf{v}_{c'}$ . Then, Eq. (9) becomes (only considering the logarithm)

$$\begin{aligned} \ln \left( \frac{\mathbf{v}_y^T \mathbf{d}(\mathbf{x})}{\mathbf{v}_{c'}^T \mathbf{d}(\mathbf{x})} \right) &= \ln(\mathbf{v}_y^T \mathbf{d}(\mathbf{x})) - \ln(\mathbf{v}_{c'}^T \mathbf{d}(\mathbf{x})) \\ &= \ln(d_{k_y}(\mathbf{x})) - \ln(d_{k_{c'}}(\mathbf{x})) \\ &= \frac{d_E(\mathbf{x}, \mathbf{w}_{k_{c'}})}{\sigma_{k_{c'}}} - \frac{d_E(\mathbf{x}, \mathbf{w}_{k_y})}{\sigma_{k_y}}. \end{aligned}$$

**If the requiredness is uncertain the output probability will it be as well.** If  $\mathbf{r}_c = \frac{1}{2}\mathbf{1}$ , then  $p_c(x) = \frac{1}{2}$ . This is an interesting result as it states that if there is no tendency in the requiredness, there is also uncertainty in the output probability, no matter how good the detection is or what the prior learns. This also states that the network could produce a constant output. In practice, we have never observed this behavior.

	CUB		CARS		PETS	
	ResNet50	ConvNeXt	ResNet50	ConvNeXt	ResNet50	ConvNeXt
number of components	2000	768	2000	768	2000	768
batch size pre-training	80	128	80	128	80	128
batch size fine-tuning and end-to-end	64	64	64	64	64	64
learning rate pre-training	$2.25e^{-4}$	$3.75e^{-4}$	$2.25e^{-4}$	$2.25e^{-4}$	$6.25e^{-5}$	$1.75e^{-4}$
learning rate fine-tuning	$4.50e^{-4}$	$5.00e^{-3}$	$2.25e^{-4}$	$5.00e^{-3}$	$1.25e^{-4}$	$5.00e^{-3}$
learning rate end-to-end	$2.25e^{-4}$	$3.75e^{-4}$	$2.25e^{-4}$	$2.25e^{-4}$	$6.25e^{-5}$	$1.75e^{-4}$
epochs pre-training	14	12	14	12	14	12
epochs fine-tuning	96	48	96	48	96	48
epochs end-to-end	144	84	144	84	144	84

Table 4: Deep CBC training parameters.

	CUB	CARS	PETS
PIPNet-C	$84.3 \pm 0.2$	$88.2 \pm 0.5$	$92.0 \pm 0.3$
PIPNet-R	$82.0 \pm 0.3$	$86.5 \pm 0.3$	$88.5 \pm 0.2$
CBC pos. reas.	$28.6 \pm 0.8$	$25.3 \pm 2.3$	$69.5 \pm 5.1$
ProtoPool	$85.5 \pm 0.1$	$88.9 \pm 0.1$	$87.2^* \pm 0.1$
ProtoViT (CaiT-XXS 24)	$85.8 \pm 0.2$	$92.4 \pm 0.1$	$93.3^* \pm 0.2$
CBC-C	<b><math>87.8 \pm 0.1</math></b>	<b><math>93.0 \pm 0.0</math></b>	<b><math>93.9 \pm 0.1</math></b>
CBC-R	$83.3 \pm 0.3$	$92.7 \pm 0.1$	$90.1 \pm 0.1$
CBC-R Full	$82.8 \pm 0.3$	$92.8 \pm 0.1$	$89.5 \pm 0.2$

Table 5: Accuracy results with different models.

## D Extended Experimental Results

This section presents the extended experimental results. For training and evaluation, we used the following hardware and software:

- Nvidia Tesla V100 GPU with 32 GB memory;
- Intel Xeon Silver 4114 (2.20 GHz) CPU with 128 GB memory;
- Ubuntu Focal Fossa (20.04 LTS) operating system;
- Python 3.10.11;
- PyTorch 2.4.0 with CUDA 12.1.

### D.1 Interpretability and performance assessment: Comparison with PIPNet

We trained our deep CBCs by following the protocol of Nauta et al. (2023). This includes

- pre-training with different loss functions (self-supervised and supervised),
- training with two different supervised training stages consisting of only fine tuning the reasoning probabilities followed by partial training of our CBC head with backbone layers (single Adam optimizer), and
- only optimizing the margin loss with  $\gamma = 0.025$ .

The remaining parameters can be found in Tab. 4. In the following, we present the complete accuracy comparison with PIPNet and ProtoPool. Then, we analyze the interpretability of PIPNet on other samples to demonstrate that the interpretation can be misleading. After that, we analyze the learned components of a CBC and discuss the limitations of the interpretability of CBC. It should be noted that the deep CBC models are only partially interpretable since the feature backbone is a black box. Therefore, it is not always possible to explain the reasoning process conclusively, as shown in the last experiment.

**ConvNeXt is better than ResNet in terms of accuracy.** Like the PIPNet experiments, we trained our CBC with a ConvNeXt-tiny (denoted by C) and ResNet50 (denoted by R) backbone. Additionally, we analyzed the impact of full backbone training instead of only training a few last layers (denoted by CBC-R Full). Tab. 5 presents the accuracy results of our method in comparison with ProtoPool and PIPNet.

First, it must be noted that our approach outperforms all the other methods and, hence, sets a new benchmark performance. The full training of a network is less effective than partial training (cf. CBC-R Full with CBC-R). Consequently, training only the few layers selected by Nauta et al. (2023) is sufficient.

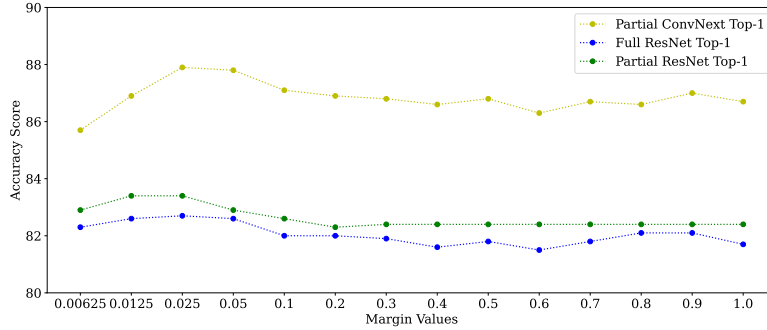


Figure 5: Margin value hyperparameter search for different backbone architectures.

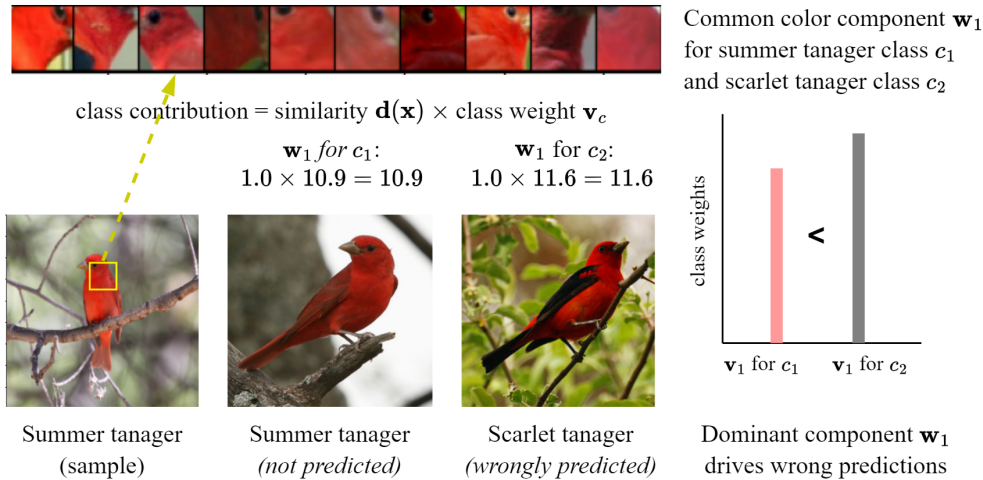


Figure 6: Issues of PIPNet with component sparsity while differentiating classes.

We also analyzed the impact of the margin parameter on the model training. For this, we trained several CBCs with different margin values. Fig. 5 summarizes the results. As we can see, the margin value has an impact on the achievable performance, but the parameter is not critical with respect to training stability. Based on this result, we selected our chosen margin value of 0.025. We performed a similar analysis with the alignment loss value. It neither improved the accuracy nor changed the top-10 component visualizations from the training dataset.

**Analysis of interpretability with PIPNet.** Here, we extend our discussion on the aspects of interpretability with respect to PIPNet. First, with Fig. 6, we demonstrate that enforced sparsity without a constraint over the weights can be problematic. For example, scarlet and summer tanagers have similar head color pattern regions but differently colored winged feathers. Because of the artificially enforced sparsity, a commonly shared component becomes more relevant for scarlet tanager, leading to image misclassification. Note that such a result is only possible because the weights are unbalanced. If the weights were constrained to probability vectors, there would likely be a tie. Fig. 7 further analyzes this issue. Here, we plot the statistics of the weights of different classes of PIPNet. The plot shows that PIPNet uses highly different weight statistics to classify classes, which further provides evidence for the hypothesized issue in Sec. 2 that less important prototypes are overemphasized.

**Learning contextually relevant components.** We utilize Fig. 8 to highlight an interesting property of CBCs: learning contextually relevant information for positive and negative reasoning. Here, for example, when classifying the given sample as a cardinal bird, the head region is selected and compared with similarly extended features around the head region for positive reasoning, and, for comparison, the head feather features learned by the component are independent of the bird species. For negative reasoning, the absence of information on water bodies from the background is used to create evidence that the input cardinal bird sample is found in non-coastal regions like forests. Thus, we observe that CBC learns to exploit background information to make predictions based on the input data distribution trends, such as cardinal birds often having non-coastal regions as background in the CUB dataset.

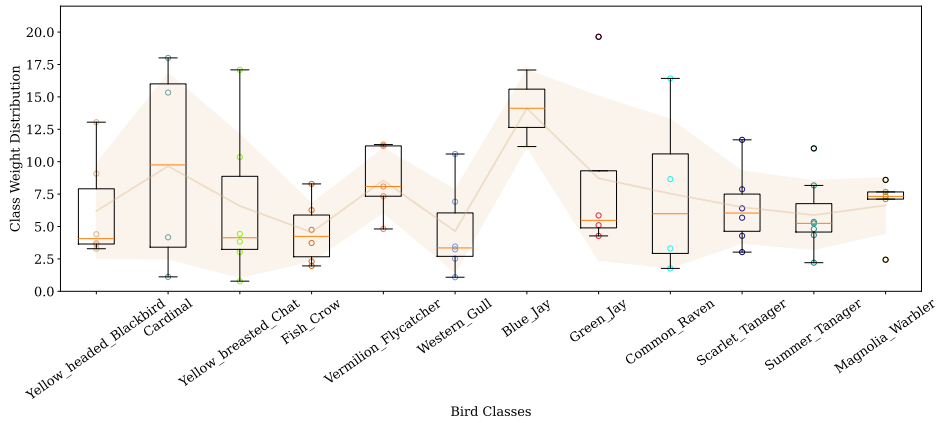


Figure 7: Unbalanced weight distribution of PIPNet. The image shows the box plots of the weights of different classes, including the mean values (solid line) and the standard deviation (shaded area).

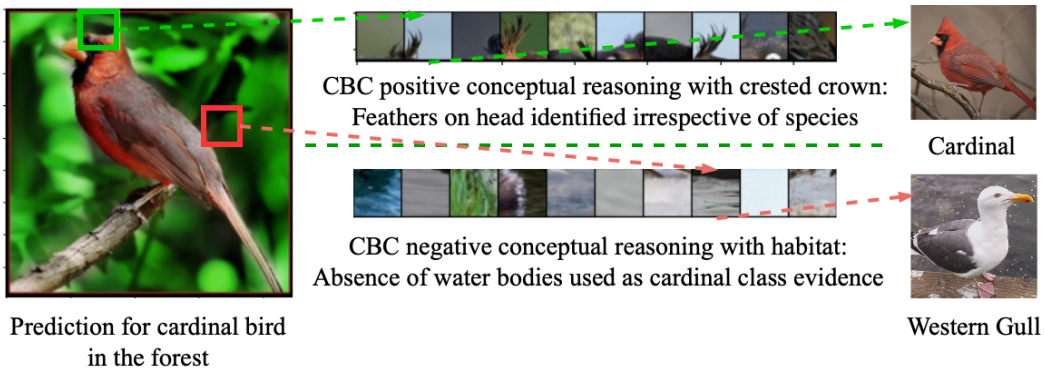


Figure 8: CBCs learning contextually relevant components for positive and negative reasoning.

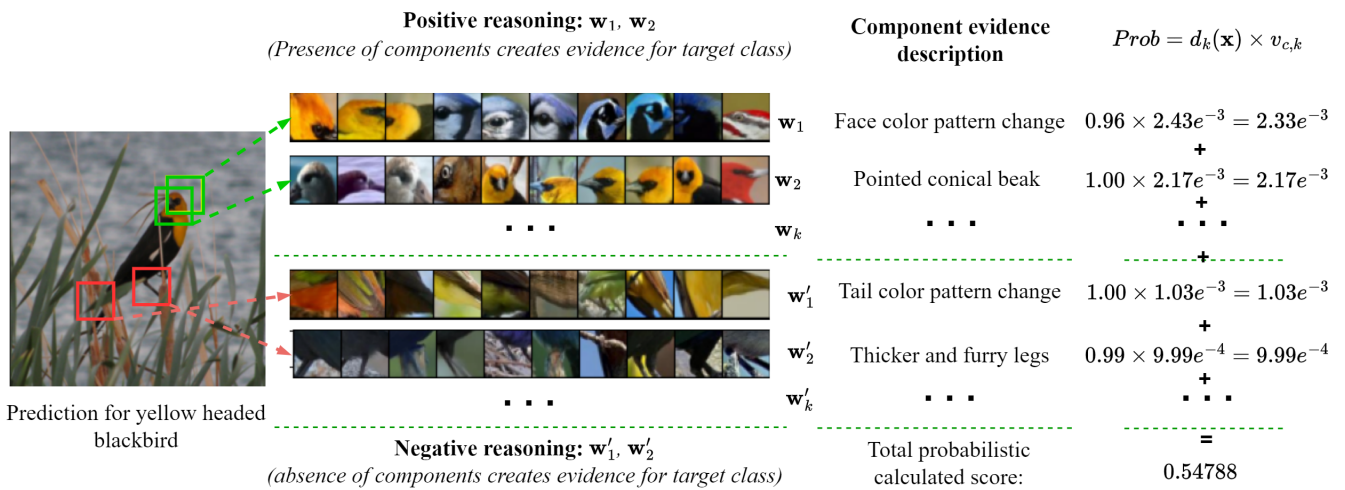


Figure 9: Probabilistic prediction mechanism of CBCs with positive and negative component contributions.

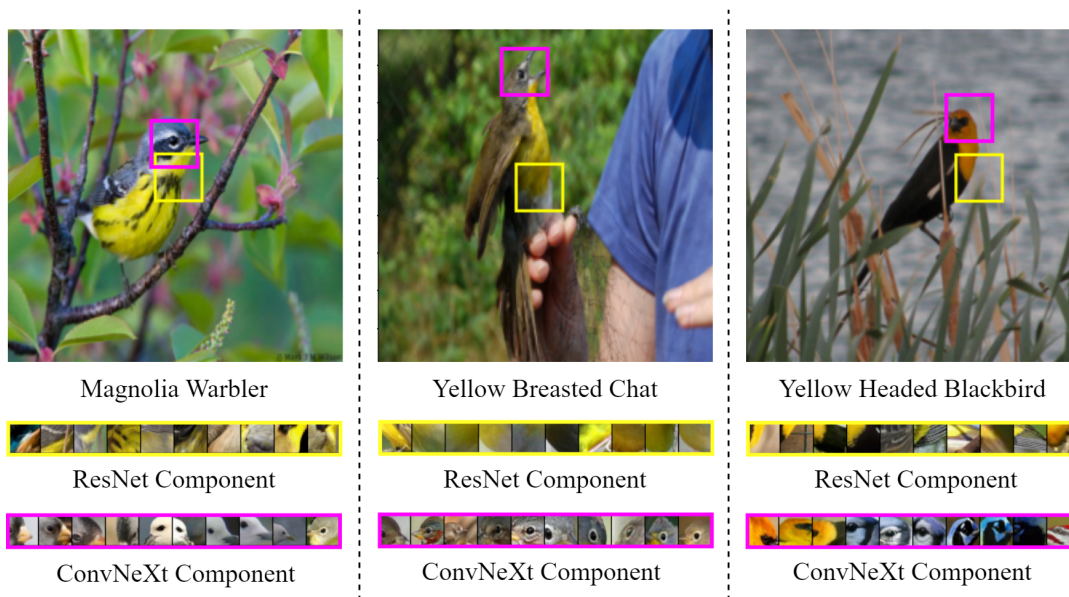


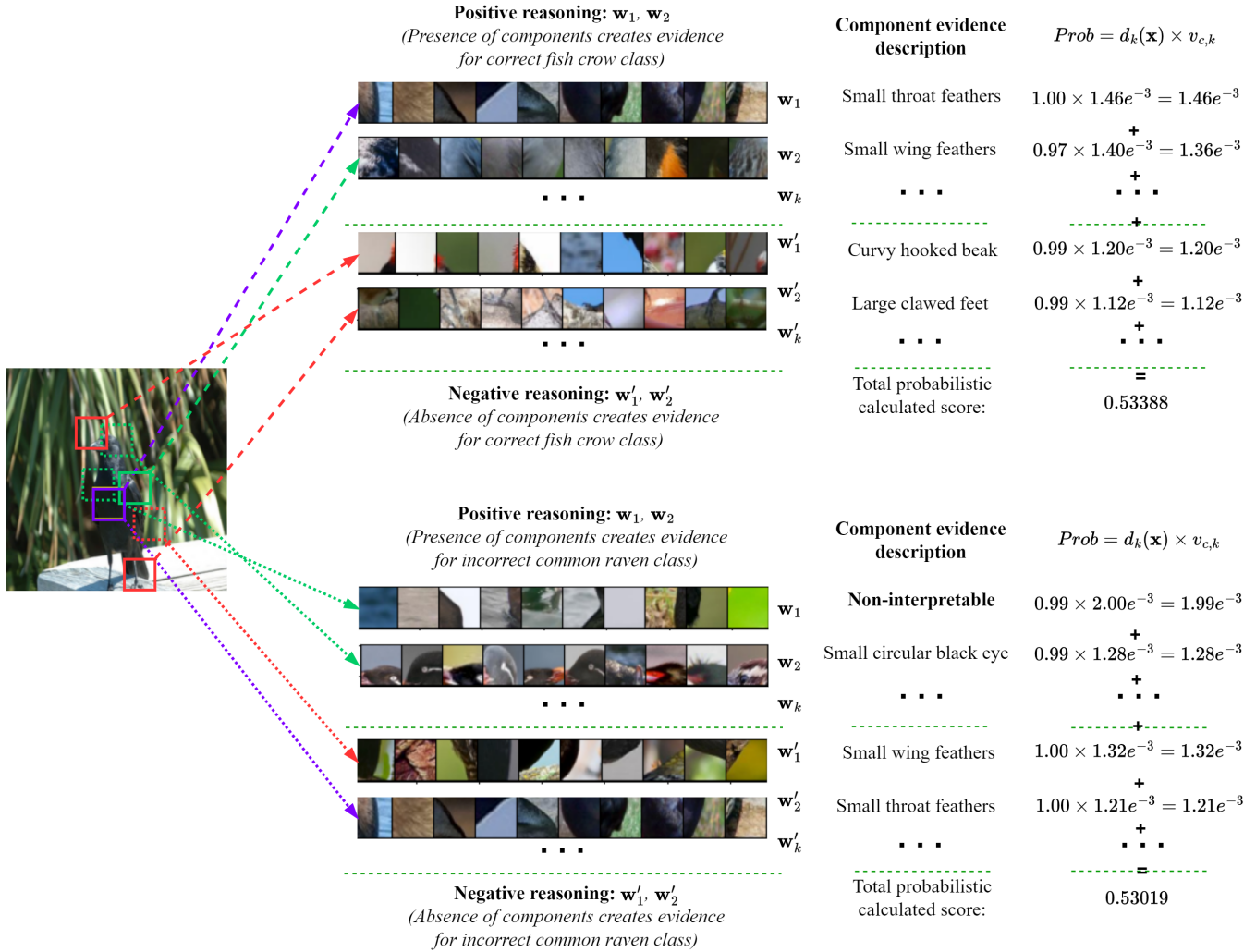
Figure 10: Comparing positive reasoning components for ResNet and ConvNeXt feature extractor backbones for CBCs.

**Limitations of interpretability with deep CBCs.** In Fig. 9, we highlight the numerical mechanism behind the qualitative analysis we presented for CBCs. We observe that the learned CBC component represents contextually relevant information independent of the bird species. However, we also state that these component representations have *non-interpretable* aspects. For example, we cannot explain why the first positive component is more important than the second one. And, in the case of bird samples and background features overlapping rectangular patches, we are often not sure whether the network utilized the bird or background features as prediction contributors. We also observe that individual negative reasoning component magnitudes are often less than individual positive components, but still, their contribution is highly important in making correct predictions. For example, we observe that the ResNet50 feature extractor with 2000 components compared to 768 components of ConvNeXt-tiny rarely uses negative reasoning. This frequently results in less reliable predictions for ResNet50 compared to ConvNeXt-tiny, which leverages negative reasoning. Moreover, with additional components, ResNet50 tends to learn color region-like components similar to PIPNet in addition to learning contextually relevant components like CBC, as demonstrated in Fig. 10. But, as evidenced by our interpretability analysis and higher performance by ConvNeXt-tiny backbone, these similar color region components are less reliable than negative reasoning components for the prediction task.

**Analysis of the prediction process for two similar classes with deep CBC.** Finally, in Fig. 11, we summarize all the relevant aspects of the prediction mechanism of the CBC approach. Here, we observe that our approach analyzes all the critical features needed to distinguish between crow and raven classes, like beak type, feather feature patterns, and foot claw variations. For the raven class, these features are more pronounced than those of crows. For negative reasoning components, given that CBCs predict for the crow class, we observe that hook-like curvy beaks and large clawed feet are used as the top negative reasoning features to create evidence for the crow class with the absence of such features in the input sample. For positive reasoning components, we observe that smooth feather patterns around the throat and wing region are used to create evidence for the crow class.

We also analyze the components of CBC prediction for wrong raven class prediction given the crow sample. In this case, we observe that the same smooth throat region component used to create positive reasoning evidence for the crow class is now used for negative reasoning to generate evidence for the raven class. Another component highlighting smooth and smaller wing feathers is again used for negative reasoning, which is opposite to what we observe for the crow class prediction. Also, for positive reasoning, we observe that a non-interpretable component is used for raven class prediction as the top contributor with the highest magnitude among correct crow class prediction and wrong raven class prediction components. However, the weight summation constraint for probabilistic interpretations and reliance on multiple components for predictions assist our methods to reduce misclassification. Empirically, reliance on several components for both positive and negative reasoning helps our approach to make robust predictions even when noisy and non-interpretable components are included as the prediction contributors.

Reliance on multiple components drives the approach towards correct prediction and gives prediction stability against non-interpretable noisy components



Same "simple throat feathers" components  $w'_1$  for common raven and  $w_1$  for fish crow are used for negative and positive reasoning for respective classes

Figure 11: Probabilistic prediction mechanism analysis of the CBC approach for the classes fish crow and common raven given a fish crow sample.

## D.2 Comparison with shallow models

We trained and evaluated all the models on the official MNIST training and test dataset using the following setting:

- epochs: 40;
- batch size: 128;
- one  $\sigma$  or several trainable  $\sigma_k$  with initial values of 58 determined by Eq. (34);
- margin value  $\gamma$  of 0.3 in Eq. (2) as proposed by Saralajew et al. (2019);
- margin value  $\gamma$  of 1.58 for robustified training (margin loss over the robust loss), which equals the commonly selected attack strength for MNIST (e. g., Voráček and Hein 2022);
- number of components or prototypes: 20;
- number of prototypes or reasoning probabilities per class: 2;
- subspace dimension  $r = 12$  for tangent distance Eq. (10) models;
- AutoAttack (Croce and Hein 2020) with the standard setting and  $\varepsilon = \{0.5, 1, 1.58\}$ ;
- *no* data augmentation;
- Adam optimizer (Kingma and Ba 2015) with learning rate of 0.005;
- all components (prototypes), except affine subspace components (prototypes), are constrained to be from  $[0, 1]^{28 \cdot 28}$  via clipping after each update step (all learned components and prototypes are valid images);
- the basis representations  $\mathbf{W}$  of the tangent distance are parameterized by the approach of Mathiasen et al. (2020);
- MNIST unit8 images are converted to float  $[0, 1]^{28 \cdot 28}$  by dividing by 255;
- all parameters are *initialized with random numbers* from a uniform distribution on the interval  $[0, 1)$ .

To analyze our proposed models and derived theorems, we trained each model with the following distances:

- squared and non-squared Euclidean distance;
- squared and non-squared tangent distance (abbreviated by TD in Tab. 6).

Moreover, we use the following baseline models with the following settings:

- **GLVQ** (Sato and Yamada 1996): This standard prototype-based model gives the baseline for prototype-based learning (prototypes are preassigned to classes and the winner-takes-all rule is applied). **GTLVQ** (Saralajew, Holdijk, and Villmann 2020) is the GLVQ version with the tangent distance. The models are trained by minimizing the GLVQ loss (Sato and Yamada 1996).
- **RBF** (Broomhead and Lowe 1988): Since our models are closely related to RBF networks, we use these models to determine the benchmark for our models without interpretability constraint. The models are trained by the cross-entropy loss and the components are considered as trainable parameters (update via stochastic gradient descent).
- **Original CBC** (Saralajew et al. 2019): Our network is an extension of this approach. Hence, we use this network type to analyze the impact of our extension. The models are trained with the margin loss.

We evaluate the following proposed models:

- **CBC**: Our proposed CBC extension trained with margin loss.
- **RBF-norm**: An RBF network where we constrain the class weights to probability vectors. By this step, an RBF network becomes a CBC where only positive reasoning is used which is interpretable. Similar to standard RBF networks, we train this model with the cross-entropy loss.
- **Robust CBC**: Our proposed CBC extension with the robustness loss is clipped at the respective margin.
- **Robust RBF**: Similar to RBF-norm but trained with the proposed robustness loss.

With this setting, Tab. 6 presents the full version of Tab. 3, where we used component-wise, trainable temperatures. In the following, we extend the discussion of the results by considering the evaluation of the models against the full set of baselines. Moreover, to analyze certain observations, we also computed the results for models where the trainable temperature was shared among all components (see Tab. 7) and where we scaled the robustness loss Eq. (33) differently (see Tab. 8). Additionally, we show in the last experiment how a patch-component-based model can be created. We interpret the reasoning process of this model and show how it automatically learns the two different concepts of the digit seven. It should be noted that the interpretation of these shallow models relies on a suitable visualization (representation of the extracted information) for the end user. Moreover, if the model becomes too large, then, similar to decision trees, the interpretation can be complicated.



	Accuracy	$\varepsilon = 0.5$		$\varepsilon = 1.0$		$\varepsilon = 1.58$	
		Emp. Rob.	Cert. Rob.	Emp. Rob.	Cert. Rob.	Emp. Rob.	Cert. Rob.
GLVQ	$79.5 \pm 0.5$	$70.2 \pm 0.5$	$56.4 \pm 0.4$	$58.8 \pm 0.3$	$32.4 \pm 0.3$	$44.1 \pm 0.3$	$14.7 \pm 0.3$
	$80.5 \pm 0.6$	$71.2 \pm 0.6$	$57.0 \pm 0.4$	$59.6 \pm 0.3$	$32.3 \pm 0.3$	$44.6 \pm 0.4$	$14.0 \pm 0.4$
RBF	$85.2 \pm 0.7$	$73.0 \pm 0.7$	–	$57.0 \pm 0.6$	–	$38.2 \pm 1.3$	–
	$92.2 \pm 0.1$	$82.0 \pm 0.1$	–	$61.9 \pm 0.9$	–	$29.9 \pm 1.7$	–
original CBC	$70.0 \pm 1.6$	$59.5 \pm 2.4$	–	$48.0 \pm 3.2$	–	$36.0 \pm 2.3$	–
	$81.8 \pm 2.0$	$72.9 \pm 1.5$	–	$62.0 \pm 1.0$	–	$46.9 \pm 0.4$	–
GTLVQ	$92.9 \pm 0.4$	$87.6 \pm 0.4$	$81.5 \pm 0.7$	$79.7 \pm 0.7$	$63.2 \pm 1.1$	$66.2 \pm 0.7$	<b><math>37.3 \pm 0.9</math></b>
	$94.1 \pm 0.3$	$89.2 \pm 0.5$	<b><math>83.0 \pm 0.7</math></b>	$81.4 \pm 0.6$	<b><math>63.7 \pm 1.3</math></b>	<b><math>67.8 \pm 0.8</math></b>	$35.5 \pm 1.0$
RBF TD	$96.5 \pm 0.1$	$91.7 \pm 0.1$	–	$81.8 \pm 0.2$	–	$60.0 \pm 0.5$	–
	<b><math>97.8 \pm 0.1</math></b>	<b><math>92.9 \pm 0.2</math></b>	–	$80.0 \pm 0.4$	–	$48.0 \pm 1.4$	–
original CBC TD	$92.5 \pm 0.1$	$87.1 \pm 0.2$	–	$78.8 \pm 0.3$	–	$65.2 \pm 0.4$	–
	$95.0 \pm 0.4$	$90.5 \pm 0.6$	–	<b><math>82.7 \pm 0.8</math></b>	–	$67.0 \pm 0.6$	–
CBC	$77.6 \pm 0.6$	$66.5 \pm 0.5$	$44.8 \pm 0.8$	$54.6 \pm 0.4$	$23.8 \pm 0.4$	$41.9 \pm 0.3$	$9.1 \pm 0.3$
	$87.4 \pm 0.3$	$79.1 \pm 0.6$	$32.3 \pm 1.8$	$68.1 \pm 0.7$	$0.2 \pm 0.1$	$52.2 \pm 0.6$	$0.0 \pm 0.0$
RBF-norm	$72.3 \pm 0.2$	$63.9 \pm 0.1$	$47.8 \pm 0.2$	$54.3 \pm 0.2$	$25.5 \pm 0.2$	$41.6 \pm 0.1$	$9.5 \pm 0.1$
	$77.3 \pm 0.2$	$68.3 \pm 0.1$	$27.8 \pm 0.2$	$57.7 \pm 0.2$	$0.7 \pm 0.0$	$43.4 \pm 0.2$	$0.0 \pm 0.0$
CBC TD	$92.5 \pm 0.1$	$87.1 \pm 0.2$	$54.0 \pm 0.6$	$78.8 \pm 0.4$	$2.3 \pm 0.5$	$65.3 \pm 0.2$	$0.0 \pm 0.0$
	<b><math>95.9 \pm 0.1</math></b>	<b><math>91.9 \pm 0.2</math></b>	$0.0 \pm 0.0$	<b><math>84.5 \pm 0.2</math></b>	$0.0 \pm 0.0$	<b><math>68.5 \pm 0.4</math></b>	$0.0 \pm 0.0$
RBF-norm TD	$90.2 \pm 0.1$	$84.1 \pm 0.3$	$46.1 \pm 0.4$	$75.6 \pm 0.2$	$6.8 \pm 1.0$	$61.9 \pm 0.2$	$0.0 \pm 0.0$
	$92.1 \pm 0.2$	$86.4 \pm 0.2$	$0.0 \pm 0.0$	$77.8 \pm 0.4$	$0.0 \pm 0.0$	$62.9 \pm 0.4$	$0.0 \pm 0.0$
Robust CBC	$78.3 \pm 0.3$	$70.0 \pm 0.2$	$59.7 \pm 0.2$	$59.9 \pm 0.2$	<b><math>38.6 \pm 0.3</math></b>	$46.6 \pm 0.1$	<b><math>16.9 \pm 0.5</math></b>
	$87.8 \pm 0.3$	$77.4 \pm 0.3$	$50.6 \pm 0.5$	$62.8 \pm 0.3$	$15.2 \pm 1.7$	$45.3 \pm 0.4$	$0.2 \pm 0.0$
Robust RBF	$78.3 \pm 0.4$	$69.8 \pm 0.4$	$59.6 \pm 0.2$	$59.8 \pm 0.4$	$38.4 \pm 0.2$	$46.4 \pm 0.3$	$16.1 \pm 0.6$
	$85.8 \pm 0.3$	$74.0 \pm 0.5$	$46.1 \pm 0.2$	$58.3 \pm 0.6$	$12.1 \pm 0.7$	$41.2 \pm 0.5$	$0.1 \pm 0.0$
Robust CBC TD	$85.6 \pm 0.3$	$78.9 \pm 0.3$	$59.8 \pm 0.1$	$70.3 \pm 0.3$	$30.7 \pm 0.2$	$57.7 \pm 0.0$	$4.4 \pm 0.4$
	$91.9 \pm 0.3$	$83.7 \pm 0.5$	$40.7 \pm 0.7$	$70.8 \pm 0.5$	$1.6 \pm 0.2$	$52.9 \pm 0.5$	$0.0 \pm 0.0$
Robust RBF TD	$86.1 \pm 0.3$	$79.4 \pm 0.3$	<b><math>60.1 \pm 0.3</math></b>	$70.6 \pm 0.2$	$30.8 \pm 0.2$	$57.8 \pm 0.2$	$5.0 \pm 0.2$
	$91.5 \pm 0.3$	$83.6 \pm 0.4$	$38.4 \pm 0.4$	$71.2 \pm 0.3$	$1.0 \pm 0.1$	$53.5 \pm 0.1$	$0.0 \pm 0.0$

Table 6: Test, empirical robust, and certified robust accuracy of different shallow prototype-based models with *component-wise* temperatures and robustness loss scaling of  $\lambda = 1$ . The top shows prior art, and the bottom shows our models. We put the best accuracy for each category in bold. The top row always shows the results for the non-squared distances, whereas the bottom row shows the results for the squared distances.

	Accuracy	$\varepsilon = 0.5$		$\varepsilon = 1.0$		$\varepsilon = 1.58$	
		Emp. Rob.	Cert. Rob.	Emp. Rob.	Cert. Rob.	Emp. Rob.	Cert. Rob.
GLVQ	$79.5 \pm 0.5$	$70.2 \pm 0.5$	$56.4 \pm 0.4$	$58.8 \pm 0.3$	$32.4 \pm 0.3$	$44.1 \pm 0.3$	$14.7 \pm 0.3$
	$80.5 \pm 0.6$	$71.2 \pm 0.6$	$57.0 \pm 0.4$	$59.6 \pm 0.3$	$32.3 \pm 0.3$	$44.6 \pm 0.4$	$14.0 \pm 0.4$
RBF	$89.0 \pm 0.2$	$78.7 \pm 0.2$	–	$62.2 \pm 0.4$	–	$39.1 \pm 1.3$	–
	$91.9 \pm 0.1$	$81.6 \pm 0.1$	–	$61.2 \pm 1.2$	–	$28.7 \pm 1.2$	–
original CBC	$71.9 \pm 5.9$	$64.4 \pm 5.0$	–	$55.5 \pm 4.0$	–	$43.3 \pm 2.5$	–
	$80.1 \pm 2.6$	$71.7 \pm 1.8$	–	$61.3 \pm 0.8$	–	$46.8 \pm 0.4$	–
GTLVQ	$92.9 \pm 0.2$	$87.7 \pm 0.4$	$81.7 \pm 0.6$	$79.7 \pm 0.6$	$63.4 \pm 0.8$	$66.4 \pm 0.5$	<b><math>37.6 \pm 0.5</math></b>
	$94.0 \pm 0.2$	$89.3 \pm 0.4$	<b><math>83.1 \pm 0.7</math></b>	$81.5 \pm 0.6$	<b><math>63.8 \pm 0.9</math></b>	<b><math>67.9 \pm 0.5</math></b>	$35.6 \pm 0.6$
RBF TD	$97.2 \pm 0.1$	$92.9 \pm 0.1$	–	<b><math>83.1 \pm 0.2</math></b>	–	$59.7 \pm 0.7$	–
	<b><math>97.9 \pm 0.1</math></b>	<b><math>93.0 \pm 0.2</math></b>	–	$79.1 \pm 0.8$	–	$43.7 \pm 1.3$	–
original CBC TD	$92.9 \pm 0.1$	$87.5 \pm 0.1$	–	$79.3 \pm 0.2$	–	$65.8 \pm 0.2$	–
	$95.0 \pm 0.3$	$90.7 \pm 0.5$	–	$82.8 \pm 0.7$	–	$67.1 \pm 0.4$	–
CBC	$82.6 \pm 0.6$	$73.1 \pm 0.6$	$59.8 \pm 0.8$	$61.5 \pm 0.6$	<b><math>36.0 \pm 0.8</math></b>	$46.9 \pm 0.5$	<b><math>17.4 \pm 0.4</math></b>
	$86.6 \pm 0.2$	$78.0 \pm 0.3$	$49.4 \pm 0.4$	$66.6 \pm 0.2$	$5.5 \pm 0.6$	$50.9 \pm 0.2$	$0.0 \pm 0.0$
RBF-norm	$72.0 \pm 0.3$	$62.8 \pm 0.3$	$48.5 \pm 0.3$	$52.1 \pm 0.2$	$27.1 \pm 0.3$	$39.1 \pm 0.4$	$12.9 \pm 0.2$
	$74.1 \pm 0.3$	$64.8 \pm 0.3$	$35.5 \pm 0.4$	$53.9 \pm 0.2$	$8.7 \pm 0.1$	$40.4 \pm 0.2$	$0.0 \pm 0.0$
CBC TD	$93.5 \pm 0.3$	$88.4 \pm 0.5$	<b><math>63.7 \pm 1.2</math></b>	$80.6 \pm 0.7$	$16.0 \pm 0.7$	$67.2 \pm 0.8$	$0.0 \pm 0.0$
	<b><math>96.0 \pm 0.0</math></b>	<b><math>92.2 \pm 0.1</math></b>	$1.5 \pm 0.2$	<b><math>84.9 \pm 0.2</math></b>	$0.0 \pm 0.0$	<b><math>68.6 \pm 0.3</math></b>	$0.0 \pm 0.0$
RBF-norm TD	$90.0 \pm 0.2$	$84.0 \pm 0.2$	$51.1 \pm 0.2$	$74.7 \pm 0.2$	$15.4 \pm 0.4$	$60.1 \pm 0.3$	$0.0 \pm 0.0$
	$91.3 \pm 0.2$	$85.6 \pm 0.4$	$7.9 \pm 0.7$	$76.6 \pm 0.4$	$0.0 \pm 0.0$	$61.7 \pm 0.7$	$0.0 \pm 0.0$
Robust CBC	$83.5 \pm 0.5$	$73.4 \pm 0.5$	$59.9 \pm 0.3$	$61.0 \pm 0.5$	$35.1 \pm 0.6$	$45.0 \pm 0.3$	$13.0 \pm 0.5$
	$92.5 \pm 0.1$	$77.9 \pm 0.9$	$11.9 \pm 0.4$	$54.2 \pm 0.7$	$0.5 \pm 0.2$	$31.4 \pm 0.4$	$0.0 \pm 0.0$
Robust RBF	$83.6 \pm 0.3$	$73.3 \pm 0.3$	$59.7 \pm 0.1$	$60.7 \pm 0.2$	$35.0 \pm 0.3$	$44.7 \pm 0.2$	$12.8 \pm 0.4$
	$91.7 \pm 0.3$	$78.5 \pm 1.1$	$29.6 \pm 0.7$	$58.5 \pm 1.5$	$1.3 \pm 0.1$	$35.3 \pm 0.9$	$0.0 \pm 0.0$
Robust CBC TD	$89.6 \pm 0.2$	$82.9 \pm 0.2$	$61.0 \pm 0.2$	$73.6 \pm 0.2$	$29.3 \pm 0.3$	$59.3 \pm 0.2$	$3.1 \pm 0.3$
	$95.7 \pm 0.2$	$89.3 \pm 0.4$	$17.6 \pm 0.8$	$76.6 \pm 0.5$	$0.0 \pm 0.0$	$55.3 \pm 0.7$	$0.0 \pm 0.0$
Robust RBF TD	$89.8 \pm 0.2$	$82.9 \pm 0.2$	$61.1 \pm 0.2$	$73.5 \pm 0.2$	$29.1 \pm 0.4$	$59.4 \pm 0.2$	$3.4 \pm 0.4$
	<b><math>96.0 \pm 0.1</math></b>	$89.6 \pm 0.2$	$13.4 \pm 1.1$	$77.3 \pm 0.4$	$0.0 \pm 0.0$	$56.2 \pm 0.3$	$0.0 \pm 0.0$

Table 7: Test, empirical robust, and certified robust accuracy of different shallow prototype-based models with *one* trainable temperature shared between all components and robustness loss scaling of  $\lambda = 1$ . The top shows prior art, and the bottom shows our models. The top row always shows the results for the non-squared distances, whereas the bottom row shows the results for the squared distances. We put the best accuracy for each category in bold.

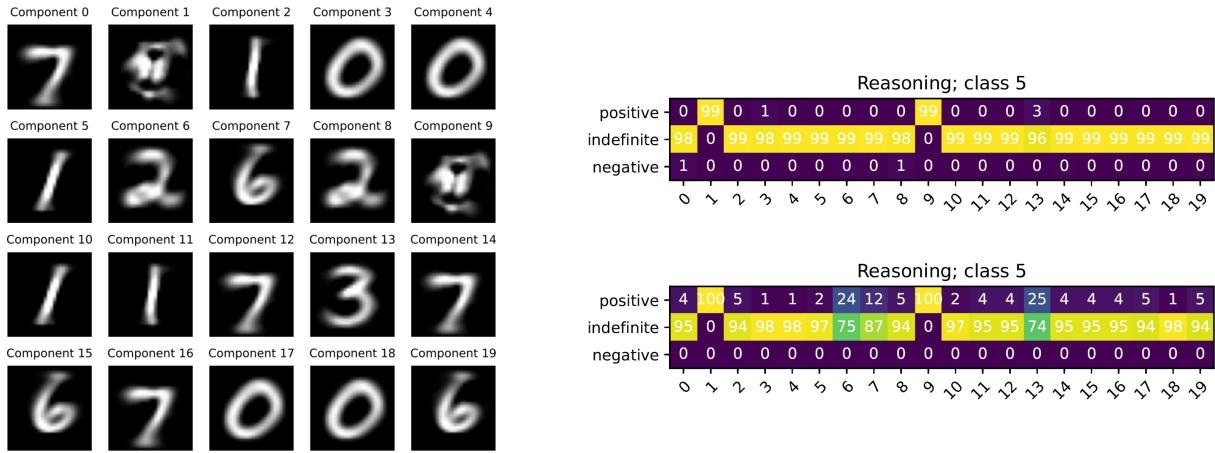


Figure 12: Learned reasoning of the original CBC. The reasoning matrix shows for each component the learned probabilities. Please note that the values displayed are rounded, which is why they may not add up to exactly 100 %.

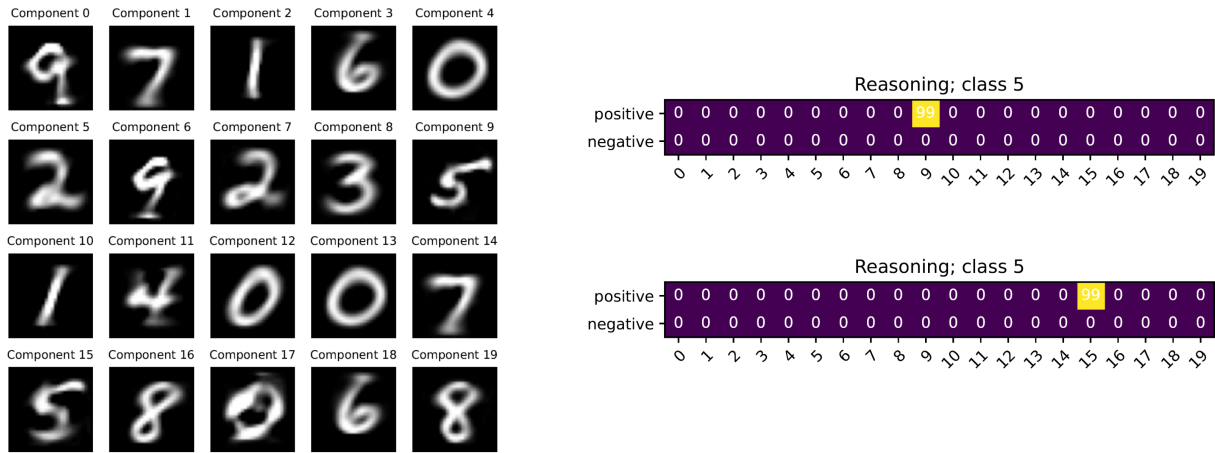


Figure 13: Learned reasoning of our CBC. The reasoning matrix shows for each component the learned probabilities.

**Negative reasoning improves accuracy.** If we compare RBF-norm with CBC for both the Euclidean and the tangent distance in Tab. 6 and 7, we can observe, in all cases, an accuracy increase. Therefore, we conclude that negative reasoning fosters accuracy. The same trend is almost always observed when we compare our CBC (or CBC TD) with GLVQ (or GTLVQ). The only violation happens for non-squared distances and component-wise temperatures (see 6), which can be explained by diverged components during training after visual inspection. This underlines the importance of a suitable temperature initialization and indicates that our proposed approach might be too simplistic.

In general, only RBF networks outperform our proposed approach. However, it should be noted that, compared to GLVQ or our models, an RBF network suffers from the mentioned interpretability shortcomings (see Sec. 2). Moreover, squared distances achieve a higher accuracy.

**Our CBC fixes the issue of original CBC.** Both CBC variants are interpreted by analyzing the learned reasoning probabilities and components. In the original CBC approach, the reasoning consists of positive, negative, and indefinite. Moreover, the component prior is set to be uniform over the number of components. Hence, following Saralajew et al. (2019), the reasoning is visualized in the form of a matrix by showing the probabilities without the component prior. Thus, the visualized probabilities in Fig. 12 sum component-wise to 100 %. For our CBC, the reasoning probabilities inherently depend on a usually non-uniform component prior. This results in reasoning matrices where the sum of all values adds up to 100 %, see Fig. 13.

Fig. 12 and 13 show the reasoning concepts learned for the digit *five*. For the original CBC, we can see, by inspecting the components, that it learned automatically class-specific components, but several components are repetitions. For instance, all learned components that represent a digit *zero* are identical. Only for the digit *one*, the components are different. Moreover, it should be noted that the model has not learned class-specific components for the digits *four*, *five*, *eight*, and *nine*. So one question is how does it differentiate between these classes. By analyzing the other reasoning matrices for these digits, we can conclude

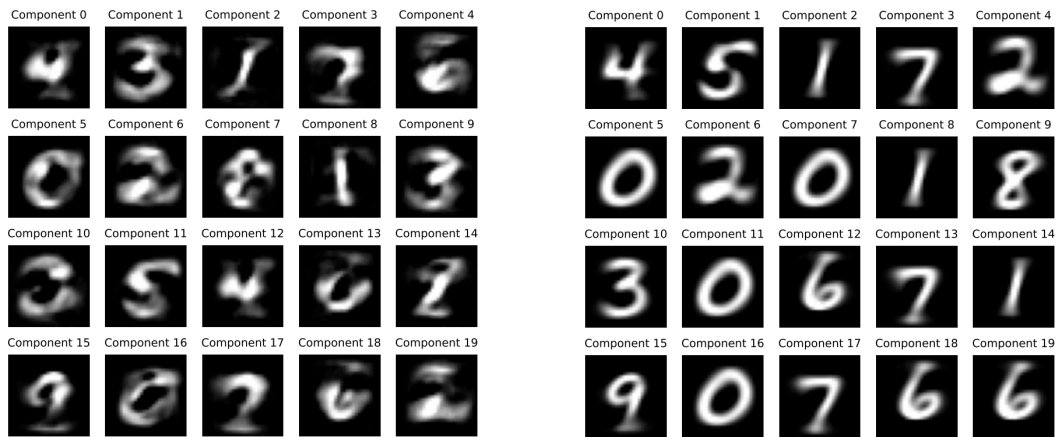


Figure 14: Components learned by an RBF (left) and by an RBF-norm (right).

that they are almost identical. Therefore, over these four classes, the original CBC does more or less random guessing. This also explains why the accuracy is around 70% (non-squared distance). Overall, this presented example demonstrates the issue of the original CBC converging to bad local minima.

On the other hand, our CBC learns different writing styles (concepts) of a five and uses these concepts since there is one reasoning matrix for each writing style of a five. However, even our model can learn repetitions of components, as shown in Fig. 13. It should also be noted that our model learned a sparse representation by only optimizing the margin loss *without* any additional regularization for sparsity. The reason why this happens can be explained by the theoretical consideration about when the optimal output probabilities are achieved, see Appx. C, which is exactly the case when the reasoning becomes crisp.

If we analyze the effect of our interpretability constraint on RBF networks, we see that the interpretability constraint promotes the interpretability of the components, see Fig. 14. However, we still encounter the issue of component repetitions even if each class is represented. For squared distances, the results are similar.

**Advanced distance measures improve the accuracy.** The results in Tab. 6 present that an advanced dissimilarity function, such as the tangent distance, constantly improves the performance of the classifiers. This underlines that the selection of a suitable distance measure is of utmost importance to build suitable classifiers with these shallow models.

**Concept learning by shallow patch models.** It is possible to build shallow patch prototype models. For this, we train our CBC with a non-squared tangent distance of patch size  $7 \times 7$  and subspace dimension 4. The tangent distance computation is applied like a convolution operation so that we get the distance responses at several pixel positions. After this, similar to deep PBNs, we compute the pixel-wise similarity according to Eq. (5) and take the maximum over all pixel with respect to each component. Then, we apply the reasoning probabilities. The entire network is trained end-to-end and follows the training setting of the other shallow models.

Fig. 15 shows the learned reasoning concepts. In the middle, we see the learned translation vectors of the learned affine subspaces. Because the components are affine subspaces, they are, to some extent, transformation invariant so that small transformations such as small rotations can be modeled. On the left and right, we see the two learned reasoning concepts for the digit *seven*. Below each reasoning concept, we show a sample from the MNIST dataset that is classified by this concept. Additionally, we show where the components get activated in the input and highlight whether they are used for positive reasoning. If we plot multiple correctly classified samples for each concept, then the split between the American and the European writing style of the digit seven becomes obvious.

With the components and the reasoning concepts, we can now interpret the classification process: For the American seven, the CBC uses one component for positive reasoning to detect the upper right corner and two components that represent circles for the “detection” that no circles are in the input, for instance, to avoid confusions with a nine. For the European seven, component 3 can detect the cross in the middle of the seven. Additionally, component 6 detects whether there is a left-sided line ending. Moreover, component 17 analyzes if there is an upside-down “T.” Finally, the reasoning also checks that there are no curved parts in the input.

By visualizing the components and reasoning probabilities in that way, the method can be interpreted. Moreover, it can also be analyzed why an input was incorrectly classified by visualizing the paths of disagreement (see dashed paths in Fig. 2), which is related to visualizing the model confusion. This was already used by Saralajew et al. (2019) to explain the success of an adversarial attack.



	Accuracy	$\varepsilon = 0.5$		$\varepsilon = 1.0$		$\varepsilon = 1.58$	
		Emp. Rob.	Cert. Rob.	Emp. Rob.	Cert. Rob.	Emp. Rob.	Cert. Rob.
Robust CBC	$87.2 \pm 0.5$	$75.8 \pm 1.0$	$48.6 \pm 0.4$	$60.6 \pm 1.1$	<b><math>16.3 \pm 0.5</math></b>	$44.7 \pm 0.6$	<b><math>0.2 \pm 0.1</math></b>
	$92.5 \pm 0.1$	$77.9 \pm 0.9$	$11.9 \pm 0.4$	$54.2 \pm 0.7$	$0.5 \pm 0.2$	$31.4 \pm 0.4$	$0.0 \pm 0.0$
Robust RBF	$87.9 \pm 0.3$	$77.9 \pm 0.5$	<b><math>51.2 \pm 0.6</math></b>	$63.8 \pm 0.7$	$15.5 \pm 1.0$	$46.2 \pm 0.9$	<b><math>0.2 \pm 0.0</math></b>
	$91.7 \pm 0.3$	$78.5 \pm 1.1$	$29.6 \pm 0.7$	$58.5 \pm 1.5$	$1.3 \pm 0.1$	$35.3 \pm 0.9$	$0.0 \pm 0.0$
Robust CBC TD	$91.9 \pm 0.2$	$83.7 \pm 0.5$	$39.4 \pm 0.7$	$71.3 \pm 0.4$	$1.1 \pm 0.2$	$53.5 \pm 0.4$	$0.0 \pm 0.0$
	$95.7 \pm 0.2$	$89.3 \pm 0.4$	$17.6 \pm 0.8$	$76.6 \pm 0.5$	$0.0 \pm 0.0$	$55.3 \pm 0.7$	$0.0 \pm 0.0$
Robust RBF TD	$92.0 \pm 0.5$	$84.5 \pm 0.8$	$40.2 \pm 1.5$	$72.4 \pm 1.0$	$1.2 \pm 0.3$	$54.6 \pm 1.0$	$0.0 \pm 0.0$
	<b><math>96.0 \pm 0.1</math></b>	<b><math>89.6 \pm 0.2</math></b>	$13.4 \pm 1.1$	<b><math>77.3 \pm 0.4</math></b>	$0.0 \pm 0.0$	<b><math>56.2 \pm 0.3</math></b>	$0.0 \pm 0.0$

Table 8: Test, empirical robust, and certified robust accuracy of our different robustified models with *one* trainable temperature shared between all components and squared distances. The top row always shows the results for robustified models with  $\lambda = 0.09$ , whereas the bottom row shows the results  $\lambda = 1$ . We put the best accuracy for each category in bold.

### D.3 Robustness evaluation

In this experiment, we use the models from the previous section and evaluate their robustness. Additionally, we compare the robustness of our CBC with the robustified counterpart over a wide range of  $\|\varepsilon\|$  and margins and show how the robust loss training improves the robustness.

**Robustness evaluation of all considered shallow models.** Tab. 6 and 7 present the full results of our robustness evaluation. First, it should be noted that the trends observed in the main part of the paper are also true for this larger set of validation models, which is that the robustification leads to non-trivial certified robustness values. Moreover, the robustified version frequently outperforms its non-robustified counterparts with respect to empirical and certified robustness. For instance, the robustified CBC outperforms the GLVQ model for non-squared distances. This observation does not fully apply to the squared distances since we see a drop in the certified and empirical robust accuracy. This can be attributed to the additional lower bounding step, which makes the derived loss (or equation for the certificate) less tight. If we compare the robust CBCs with the robust RBF models, then we see that the robust CBC scores are almost always slightly better than the RBF. Similar to before, we attribute this observation to the effectiveness of negative reasoning.

In Tab. 8, we present the robustified accuracy for squared distance models trained with  $\lambda = 1$  and  $\lambda = 0.09$ . Since the two loss terms in the robustified loss formulation are differently scaled, the loss terms must be balanced by a regularization value. Usually, the loss term  $\delta$  for incorrect classification varies more than the loss term for correct classification. Hence, promoting less incorrect classifications if  $\lambda = 1$ . The results in Tab. 8 present exactly this behavior. By removing the scaling, the model achieves a higher accuracy but becomes less robust because more emphasis is put on minimizing the number of incorrectly classified samples.

**Robustness curves.** Fig. 16 presents the robustness curves of CBCs and Robust CBCs with the non-squared Euclidean distance, one trainable temperature, and  $\lambda = 1$ . The curves for the Robust CBC show how the optimization of the robust loss optimizes the certified robustness accuracy. If the robustification margin is too small, then the model is only provable robust for small attack strengths. With an increasing robustness margin, the robust accuracy improves over the entire attack strength range. However, this improved robustness lowers the clean test accuracy. For CBC, we see that the model shows a similar empirical robustness as Robust CBC for large margins. The maximum robustness behavior is achieved for a margin of around 0.3. After this value, there is not much improvement in the empirical robustness. Even if the network was not optimized for provable (certified) robustness, the provable robustness is almost the same for large margins.

**Discussion** Empirically, we observe that the maximization of the probability gap also generates models with non-trivial certifiable robustness. Why this happens has to be investigated. One possible explanation could be that the output probability of a CBC model reaches its maximum if the reasoning becomes crisp and, hence, becomes a GLVQ-like model. At the same time, this implies that the loss reduces to the hypothesis margin maximization (see Appx. C). To analyze this hypothesis, we determined whether the reasoning is crisp when the model shows a non-trivial robustness. The collected results showed that this hypothesis is not true since we found several cases where the model was robust, but the reasoning was not crisp. Another hypothesis we investigated is whether a larger probability gap always increases the robustness. Again, this hypothesis must be rejected for individual samples as it is easy to show that an *individual* sample can have a high margin but a small robustness. Additionally, we analyzed whether this hypothesis holds over the entire dataset on average. For this, we created a linear separable dataset and trained 1000 models that solved this dataset perfectly. For each model, we computed the average probability gap and robustness loss and checked whether they were ranked similarly. Again, we have to reject this hypothesis (analyzed with Kendall

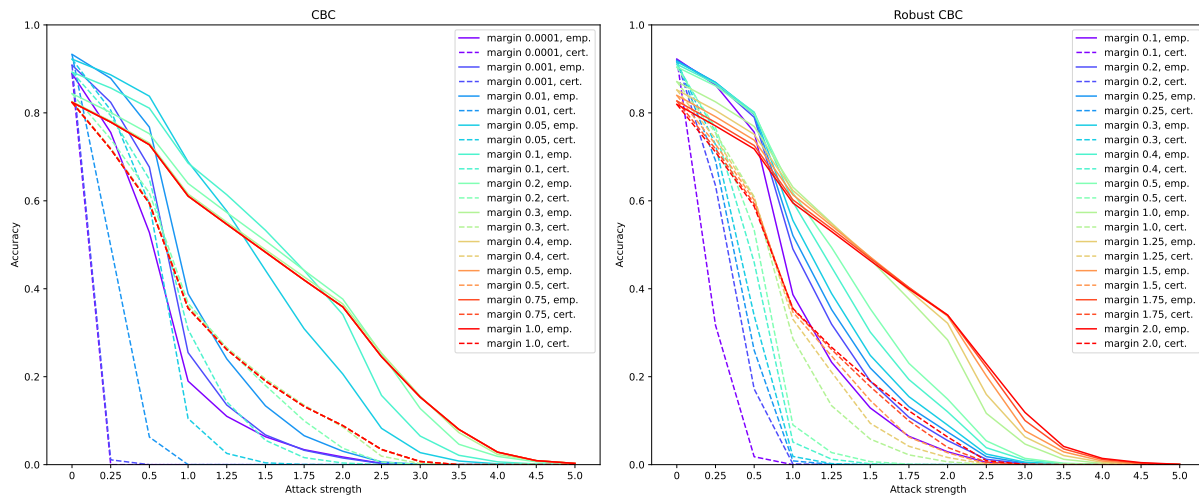


Figure 16: Robustness curves for non-squared CBC (left) and Robust CBC (right) trained with different margins and evaluated for several  $\|\epsilon\|$ .

tau rank loss)—we also found several situations on MNIST where this hypothesis is violated. Consequently, right now, it is an open problem why the probability gap maximization encourages robustness.

Also note that the true robustness of our created models might be significantly higher because the AutoAttack framework consists of strong attacks that approximate the true robustness well for shallow prototype-based models (Voráček and Hein 2022). Assuming this is true raises the question of why “non-robustified” models such as RBF and the original CBC achieve good robustness scores.